The Thesis Committee for Bryan Valmonte Riel

Certifies that this is the approved version of the following thesis:

Radiometric Calibration of High Resolution UAVSAR Data Over Hilly, Forested Terrain

APPROVED BY

SUPERVISING COMMITTEE:

Sean Buckley, Supervisor

Marc Simard

Radiometric Calibration of High Resolution UAVSAR Data Over Hilly, Forested Terrain

by

Bryan Valmonte Riel, B.S.Ase.

THESIS

Presented to the Faculty of the Graduate School of

The University of Texas at Austin

in Partial Fulfillment

of the Requirements

for the Degree of

MASTER OF SCIENCE IN ENGINEERING

THE UNIVERSITY OF TEXAS AT AUSTIN

December 2010

Radiometric Calibration of High Resolution UAVSAR Data Over Hilly, Forested Terrain

Bryan Valmonte Riel, M.S.E.
The University of Texas at Austin, 2010

Supervisor: Sean Buckley

SAR backscatter data contain both geometric and radiometric distortions due to underlying topography and the radar viewing geometry. Thus, applications using SAR backscatter data for deriving various scientific products (e.g. above ground biomass) require accurate absolute radiometric calibration. The calibration process involves estimation of the local radar scattering area through knowledge of the imaged terrain, which is often obtained through DEMs. High resolution UAVSAR data over a New Hampshire boreal forest test site was radiometrically calibrated using a low resolution SRTM DEM, and different calibration methods were tested and compared. Heteromorphic methods utilizing DEM integration are able to model scattering area better than homomorphic methods based on the local incidence or projection angle with a resultant backscatter calibration difference of less than 0.5 dB. Additionally, the impact of low DEM resolution on the calibration was investigated through a Fourier analysis of different topographic classes. Power spectra of

high-resolution airborne lidar DEMs were used to characterize the topography of steep, moderate, and flat terrain. Thus, errors for a given low resolution DEM associated with a particular topographic class could be quantified through a comparison of its power spectrum with that from the lidar. These errors were validated by comparing DEM slope derived from SRTM and lidar DEMs.

The impact of radiometric calibration on the biomass retrieval capabilities of UAVSAR data was investigated by fitting second-order polynomials to backscatter vs. biomass plots for the HH, HV, and VV polarizations. LVIS RH50 values were used to calculate biomass, and the process was repeated for both uncalibrated and area calibrated UAVSAR images. The calibration improved the R^2 values for the polynomial fits by 0.7-0.8 for all three polarizations but had little effect on the polynomial coefficients. The Fourier method for predicting DEM errors was used to predict biomass errors due to the calibration. It was revealed that the greatest errors occurred in the near range of the SAR image and on slopes facing towards the radar.

Table of Contents

List of Tables

List of Figures

Chapter 1

Introduction

Understanding the dynamics and properties of forest ecosystems plays a crucial role in balancing the global carbon budget, predicting future climate change, and quantifying the impact of human activities on the environment. Forest properties can affect human life on both regional and global scales.

The carbon cycle is primarily concerned with the exchange of carbon between the atmosphere, oceans, and the land biosphere [13]. The variability of the atmospheric CO_2 growth rate has been shown to be primarily affected by the response of the land biosphere to climate variations [13]. Furthermore, many climate models have placed the interaction between the land biosphere and other climate regions (e.g., atmosphere and cryosphere) in a positive feedback loop. For example, the level of atmospheric CO_2 is dependent upon the efficiency of the land biosphere as a carbon sink, which in turn is affected by atmosphere induced climate change. Any change in the structure of the forest ecosystems results in changes in the carbon allotment between the atmosphere and the land biosphere. All in all, the carbon cycle becomes affected when human activities are taken into account. The consensus is that CO_2 emissions are the largest anthropogenic contribution to climate change while deforesta-

tion and agriculture development are second. However, the uncertainty in the carbon flux due to land use changes (such as deforestation) is the most significant uncertainty in the global carbon budget.

One of the most important variables in the global carbon budget is forest biomass. Knowledge of the spatial distribution of biomass enables better estimates for carbon sources and sinks and allows for temporal variations to be monitored [22]. However, spatial measurements of biomass have traditionally been based on forest inventory data acquired on the ground. The sample spacing of the inventory data is often poor and fails to capture the high-resolution variation of biomass necessary to accurately calculate carbon flux. One way to account for this is to use remote sensing technologies.

Remote sensing of forests and major ecosystems has long been employed as a useful technique for monitoring landcover change and quantifying various properties, including biomass, canopy height, and canopy volume [34]. The main advantages that remote sensing provide over in situ field data are wider coverage, more efficient data acquisition methods, and lower costs. "Passive" remote sensing technologies, such as multi- and hyperspectral optical imaging, have been used to map forest extent, classify forests based on species, and estimate leaf area index (LAI) [10]. Passive sensors measure reflected/emitted radiation from other sources, such as sunlight or infrared heat. Therefore, the sensors are limited by the time of day and weather conditions. In recent years, the remote sensing community has adopted "active" technologies where radiation is emitted by the sensor and the reflected radiation from the

ground targets is recorded. The type of radiation emitted is dependent on the wavelength.

Light Detection and Ranging (LIDAR, or lidar) sensors emit near-infrared light beams towards the surface and measure the sensor-to-surface distance using the time-of-flight principle. Ranging information combined with sensor position and pointing information can yield high-resolution topographic maps. Lidar systems that actually record the full reflected waveforms can provide information on the vertical structure of forests [18]. Synthetic Aperture Radar (SAR) systems use reflected radar pulses to image the ground targets. SAR antennas are usually side-looking, and the moving platform allows for a larger antenna aperture to be synthesized, resulting in high-resolution imagery. Longer wavelengths as compared to optical and lidar remote sensing make SAR systems independent of both weather and time of day. Initial work with SAR imagery discovered that the intensity of returned SAR signals, or backscatter, over forests was positively correlated to aboveground biomass, a quantity important to understanding the carbon flux between forest ecosystems and the atmosphere [27]. Higher biomass quantities indicate more components for the radar beam to interact with and scatter off of, leading to higher backscatter values. The backscatter is also a function of radar wavelength, where longer wavelength SAR signals (L- and P-band) are able to penetrate tree canopies and are more sensitive to trunks and larger woody components. Shorter wavelength signals (C- and X-band) tend to scatter near the canopy layer. This paper will focus on the use of SAR backcscatter data to image forested areas.

In terms of ground properties, SAR backscatter data is a function of aboveground biomass, soil moisture, topography, ground roughness, et al. [1]. Furthermore, raw intensity images also inherently contain brightness variations due to antenna patterns and range spreading loss [12]. Therefore, accurate estimation of a quantity like biomass requires all other effects to be removed from the backscatter data. Backscatter variation due to topography is the single largest error source when estimating biomass over steep or hilly terrain [1]. For example, for ground slopes facing towards the radar, the reflected SAR signal has a higher intensity due to a smaller local illuminated area. On the other hand, ground targets that are in "shadow", or areas that receive little to no illumination from the radar beam, have very low intensity values. Biomass estimates for these regions incur significant errors. In order to correct radar backscatter distortions due to topography, absolute radiometric calibration must be performed. The primary purpose of radiometric calibration is to normalize the radar intensity values so that only the signal due to vegetation and surface conditions remains.

The primary research objective of this paper is to present a method to radiometrically calibrate SAR backscatter data due to topography. Different calibration methods will be examined and compared as applied to a selected SAR scene. Calibration error due to errors in topography measurements will also be discussed and estimated using a Fourier based analysis. Then, the ability of SAR to estimate biomass will be examined over a hilly, high-biomass forest in New Hampshire where radiometric distortions due to topography are

significant. Biomass estimation and accuracy will be analyzed pre- and post-radiometric calibration, and propagation of errors will be used to estimate total biomass uncertainty due to uncertainties in the topography coupled with uncertainties in the biomass estimation algorithm.

Chapter 2

Radiometric Calibration of SAR Data for Topography

Due to the side looking nature of SAR systems, topography can induce geometric and radiometric distortions in the data. Both of these distortions are primarily influenced by the local incidence angle θ_{loc}, the angle between the radar line-of-sight and the surface normal. θ_{loc} is generally defined as $\theta_{loc} = \theta_i - \alpha_s$, where θ_i is the incidence angle of a horizontal patch on the ground and α_s is the local surface slope toward the radar [1]. For many applications, radiometric distortions due to topography are the largest error sources when performing absolute radiometric calibration [1]. Generally, ground slopes facing toward the radar appear brighter in the radar image while slopes facing away are darker. The two main factors for these distortions are: 1) variations in pixel brightness due to changes in the local illuminated area, and 2) variations in backscatter due to changes in the local incidence angle [7]. However, both factors are related to the incidence angle of the SAR signal. Lower incidence angles reduce the scattering area and lead to increased radar brightness. Polarimetric decomposition methods have been applied to show that larger incidence angles result in an increased proportion of volume to surface scattering [29], which has a significant factor for the backscatter

of forested areas. Empirical backscattering models have been developed and tested for various landcover classes to attempt to correct for this change in primary backscatter mechanisms [6].

Both satellite and aircraft based SAR data contain backscatter variations, although the data acquisition parameters have different degrees of impact for each type. For instance, since aircraft data are acquired at much lower altitudes than satellite data, the range of look angles (the angle between the local vertical and the radar beam) is much wider. For the UAVSAR system operated by the Jet Propulsion Laboratory (JPL), the aircraft generally flies between 30,000-40,000 feet, leading to look angles that can vary from $\approx$20-70°. For steep topography, the large range of look angles can result in a significant portion of the target site to be in shadow. On the other hand, satellites image the ground at altitudes on the order of 700 km, resulting in look angles that vary only a few degrees from the center. The lower altitude of the UAVSAR system also results in greater sensitivities to residual motion of the aircraft and antenna, such as aircraft yaw and pitch and antenna steering angles. All in all, aircraft acquired SAR images are generally more complicated to calibrate than satellite images and require consideration of a greater number of factors.

The main objective of this chapter is to present a suitable radiometric calibration technique for calibrating high-resolution airborne SAR images using low-resolution reference digital elevation models (DEMs). For demonstration purposes, high-resolution UAVSAR intensity images are corrected using low-resolution Shuttle Radar Topography Mission (SRTM) DEMs provided

with the radar data. First, several radiometric calibration techniques to correct for the variation of the local radar illuminated area due to topography are introduced. The mathematical formula, methods, and remote sensing data used are explained for each technique. The calibration performances are compared through a combination of visual inspection of the backscatter images, construction of histograms of the backscatter values, and extraction of transects along the radar range direction.

2.1 Radiometric calibration

2.1.1 Data and Study Site

2.1.1.1 UAVSAR

The UAVSAR instrument is an L-band SAR system designed for repeat-pass interferometry, allowing for precise measurements of crustal motion, deformation events, vegetation structure, et. al. [21]. The antenna is electronically steered in order to help overcome aircraft motion due to air turbulence and other factors expected for an airborne system. While single-look complex (SLC) data are not freely distributed, quad-polarized multilooked intensity images (3 looks in range/cross-track, 12 looks in azimuth/along-track) are readily available online (`http://uavsar.jpl.nasa.gov/`). The images are formed as cross-products of the original SLC pixels where $HHHH$ indicates $S_{HH}S_{HH}^{*}$.

A single UAVSAR data strip was downloaded over the White Mountain National Forest in New Hampshire. The data was acquired on August 5, 2009 at a heading of 250° and an average altitude of 12500 m. The strip

covered an area approximately 20 km in the range direction and 100 km in azimuth. The study site itself consists of elevations ranging from 680-3000 ft with thick vegetation cover for most of the strip. Conifers are dominant at the higher elevations while a mix of conifers and high biomass hardwoods can be found lower [2]. The presence of dense vegetation causes the radar image to be particularly sensitive to radiometric distortions due to topography, and normalization by the illuminated area will only correct for half of those effects. The real valued data ($HHHH$, $HVHV$, $VVVV$) were corrected for area effects, although the $HVHV$ data is the main focus for this study. All parameters necessary for calibration were read from the metadata found in the annotation file.

2.1.1.2 SRTM DEM

SRTM was a joint mission between JPL and the National Geospatial-Intelligence Agency (NGA) in 2000. The mission used a C-band dual-antenna radar interferometer to generate a global DEM for latitudes less than 60° [42]. JPL processed the data to form the DEMS, which were released at a 1-arcsecond pixel spacing for the United States and 3-arcseconds for other regions. UAVSAR data are generally geocoded to SRTM DEMs where the DEMs are available, and the segments of the DEMs imaged by the radar are provided with the UAVSAR data. The supplied DEMs are first oversampled to a pixel spacing of 1/5-arcseconds ($\approx$ 5-6 m) before geocoding of the radar data in order to better match the native resolution of the SAR instrument.

Therefore, the DEMs may be formed from oversampling factors as high as 15. The elevation data itself is susceptible to measurement noise from the radar, geolocation errors, and biases from vegetation due to C-band signals scattering off canopies [33]. The SRTM DEM provided with the White Mountain National Forest UAVSAR data was used for calibration.

2.1.2 Calibration methods

Several different radiometric calibration approaches persist in the scientific literature. The general approach, which is common to all methods, is to estimate the local ground area illuminated by the radar beam and normalize the radar backscatter values by an area factor. In equation form, the calibration would be:

$$\sigma^\circ = \beta^\circ \frac{A_{ref}}{A} \tag{2.1}$$

where σ° is the calibrated backscatter value, β° is the uncorrected value, A_{ref} is the area of a radar pixel in the slant plane, and A is the illuminated ground area for that pixel. The main attribute that differs from method to method is the estimation of the local illuminated area. The two main philosophies are estimation of the area through either: 1) local incidence angle or some other projection angle, or 2) integration of the digital elevation model (DEM) [41, 38]. The former method has the advantage of being simpler to implement while the latter is more accurate, especially in steep terrain, but is more computationally intensive. The integration involves determining the number of DEM pixels belonging to each radar range and azimuth pixel through knowl-

edge of the geocoding process.

2.1.2.1 Homomorphic calibration: projection and incidence angles

Homomorphic calibration techniques assume a one-to-one transformation between the radar and map geometries, which is not necessarily a valid assumption under certain sensor viewing geometries; many map pixels may fall within the same radar pixels in an irreversible transformation [38]. Homomorphic calibration is performed in map geometry, and the conventional method to estimate the illuminated area of a map pixel is to use the local incidence angle, which is the angle between the surface normal vector and the look vector to the sensor [38, 17]. The surface normal is defined by the terrain slope, S, and aspect, A, which are calculated as [43]:

$$S = \arctan\sqrt{f_x^2 + f_y^2} \tag{2.2}$$

$$A = 270^\circ + \arctan\left(\frac{f_y}{f_x}\right) - 90^\circ\frac{f_x}{|f_x|} \tag{2.3}$$

where f_x and f_y are the gradients along the W-E and N-S direction, respectively, and are calculated using a 3rd order finite difference with a 3×3 moving window. The local incidence is calculated as:

$$\cos\theta_l = \sin(\alpha)\sin(S)\cos(\beta - A) + \cos(\alpha)\cos(S) \tag{2.4}$$

where α and β are the average elevation and azimuth, respectively, of the SAR sensor. Then, the ground area normalized backscatter value is:

$$\sigma^\circ = \beta^\circ \sin\theta_l \tag{2.5}$$

Use of the local incidence angle to estimate the illuminated area was derived from an ellipsoid Earth model over flatlands to normalize radar values acquired over flatlands and has been shown to not properly calibrate layover/foreshortening and shadow areas [37].

An improved homomorphic calibration technique makes use of the projection angle, which is defined as the angle between the surface normal and the normal to the imaging plane [41, 19]. It was shown by [41] that the local incidence angle area estimation is just an approximation to the projection angle derived area. For the UAVSAR system and viewing geometry parameters, the projection angle is used in the following way [19]:

$$A = \frac{\Delta\rho\Delta az}{\langle \hat{n}_\Sigma, \hat{n}_I \rangle} \tag{2.6}$$

where $\hat{n}_\Sigma$ and $\hat{n}_I$ are the unit normal vectors to the terrain and the radar imaging slant plane. The vectors are defined with respect to the radar SCH coordinate system, where $\hat{s}$ is the along-track direction, $\hat{h}$ points opposite the aircraft nadir direction, and $\hat{c}$ completes the right-handed system. The projection angle can be defined as:

$$\cos\psi = \langle \hat{n}_\Sigma, \hat{n}_I \rangle \tag{2.7}$$

To construct the unit normal to the terrain, the terrain slope must be broken into components along the range and azimuth directions [24]:

$$\tan\tau_\rho = \tan S \cos\left(A - (HEAD - 90)\right) \tag{2.8}$$

$$\tan\tau_s = \tan S \cos\left(A - HEAD\right) \tag{2.9}$$

where $HEAD$ is the aircraft heading, τ_ρ is the ground slope in the range direction, and τ_s is the ground slope in the azimuth direction. Then, the unit normal to the terrain is:

$$\hat{n}_\Sigma = \frac{-1}{\sqrt{1 + \tan^2 \tau_\rho + \tan^2 \tau_s}} \begin{bmatrix} \tan \tau_s \\ \tan \tau_\rho \\ -1 \end{bmatrix} \tag{2.10}$$

The derivation for the unit normal to the radar imaging slant plane first involves deriving an expression for the unit look vector from the sensor to the ground target. It can be shown that the look vector has the following form [21]:

$$\begin{aligned} \hat{l}_s &= \sin\alpha \cos\theta_p \cos\theta_y \\ &\quad + \cos\alpha \left(\sin\theta_p \cos\theta_i \cos\theta_y + \sin\theta_i \sin\theta_y\right) \\ \hat{l}_c &= -\sin\alpha \cos\theta_p \sin\theta_y \\ &\quad + \cos\alpha \left(-\sin\theta_p \cos\theta_i \sin\theta_y + \sin\theta_i \cos\theta_y\right) \\ \hat{l}_h &= \sin\alpha \sin\theta_p - \cos\alpha \cos\theta_p \cos\theta_i \end{aligned} \tag{2.11}$$

where θ_y and θ_p are the aircraft yaw and pitch angles, α is the electronic steering angle, and θ_i is the incidence angle of a horizontal patch on the ground. Finally, $\hat{n_I}$ can be computed as:

$$\hat{n}_I = \hat{s} \times \hat{l} \tag{2.12}$$

The projection angle method still suffers from the homomorphic assumption. To mitigate this effect, an illuminated area *image* in map coordinates was formed. Then, the image was resampled to the radar geometry

using inverse distance weighting and through knowledge of the map coordinates and the sensor position. For UAVSAR, this involved the transformation between geographic latitude/longitude to the SCH system using the peg quantities found in the annotation file (see Appendix). Finally, the correction is performed on the β° values in the radar geometry.

2.1.2.2 Heteromorphic calibration: DEM integration

A more accurate estimation of the illuminated area requires an integration of the DEM. The premise of this approach is to determine the number of DEM pixels that fall within each radar pixel by taking advantage of knowledge of the transformation between map and radar geometries. Thus, the ground area is integrated over the DEM, and no information is lost due to the homomorphic assumption. For UAVSAR, the process begins by decomposing the DEM into facets and computing the fractional range and azimuth bin corresponding to each map facet [7]. Then, a bilinear weighting model is used to distribute the facet area over the appropriate radar pixels. The integer bounds in the radar image become:

$$r_1 = \text{floor}(r), \quad r_2 = \text{ceil}(r),$$
$$a_1 = \text{floor}(a), \quad a_2 = \text{ceil}(a)$$

where r and a are the fractional range and azimuth bins, respectively. The integer bounds are used as array indices for the area image in radar coordinates.

The bilinear distribution is performed as follows:

$$A_{a_2,r_2} = A_{a_2,r_2} + (r - r_1)(a - a_1) * \text{area}$$

$$A_{a_2,r_1} = A_{a_2,r_1} + (r_2 - r)(a - a_1) * \text{area}$$

$$A_{a_1,r_2} = A_{a_1,r_2} + (r - r_1)(a_2 - a) * \text{area}$$

$$A_{a_1,r_1} = A_{a_1,r_1} + (r_2 - r)(a_2 - a) * \text{area}$$

where A is the area image in radar coordinates and the quantity (area) is the area of the facet. The correction is performed in radar coordinates using Eq. 2.1. The performance of the DEM integration for estimating area is improved through oversampling of the DEM, which improves the texture and resolution of the area image after integration. The nominal oversampled spacing should be equivalent to $\approx 1/3$ the pixel spacing of the radar image.

2.1.3 Results and Discussion

In uncalibrated radar intensity images, slopes facing toward the radar are brighter while slopes facing away are darker, which can be seen in Fig. 2.1. Application of the different calibration methods reveals the effectiveness and limitations of each (Fig.'s 2.1b-d). The main areas that are effectively calibrated for all methods are the brighter areas on slopes facing toward the radar. Slopes facing away from the radar are also adjusted, although the topographic distortion in the images largely remains. This effect is due to changes in the interaction of the radar signal with the scatterers as a result of changing incidence angles and is usually the next step in calibration after area normal-

ization [7]. Close inspection of the images reveal areas that are not sufficiently corrected by the conventional local incidence angle method. As mentioned before, this method was developed from ellipsoidal models for flatlands and is not appropriate for steep topography. The calibrated radar images from the projection angle and heteromorphic facet corrections are nearly identical.

Figure 2.2 confirms the general trend of backscatter vs. illuminated area for transects along the range direction. The values were computed from a transect extracted from one of the steeper areas of the radar scene. The uncorrected data display a strong increase in backscatter with area, while the three calibration methods result in backscatter values that are largely independent of the area up to ≈ 350 m^2. For steeper terrain and higher area values, the incidence angle correction is insufficient and the backscatter is only partially corrected. The projection angle and heteromorphic facet methods result in close agreement of calibrated backscatter values for all areas, although the projection angle calibration appears to exhibit a slight overcorrection. The overcorrection may be due to the area resampling process from map to radar coordinates. Since radiometric calibration consists of a multiplicative factor based entirely on the estimated illuminated area, further comparison of the different calibration methods can be performed by analyzing the images of the illuminated area.

Images of the illuminated area contain much of the same characteristics as actual radar images, i.e. brighter areas in the radar image correspond to areas of higher illuminated area and vice versa. By forming a reference area

image using the heteromorphic method (Fig. 2.3a), differences in calibration performance can be obtained by subtracting area images formed from each method from the reference image. Figure 2.3b shows that the incidence angle both over- and underestimates the area, particularly on higher slopes facing towards the radar. On those slopes, the homomorphic assumption is particularly prone to errors since several map pixels may be associated with the same radar pixel. The projection angle differences (Fig. 2.3c) display good agreement with the heteromorphic method and only has problems in the highest slopes facing towards the radar, where overestimation of the area occurs. Therefore, the resampling process from map to radar coordinates helps to regain the information lost due to the homomorphic assumption. By forming a histogram of the area differences (Fig. 2.4), it was found that the incidence angle method displays a bias towards underestimation of the area, while the wide peak in the normalized count indicates a widespread distribution of area errors. On the other hand, the projection angle method displays a very prominent and narrow peak near 0, which matches the results shown in Fig.'s 2.3 and 2.2. The slight overcorrection of backscatter values observed in Fig. 2.2 for the projection angle method can be explained by the slight shift towards the negative of its associated histogram in Fig. 2.4. The area differences can be propagated to a radiometric calibration difference, where it was found that the projection angle method was within 0.5 dB of the facet model for most slopes.

Overall, the calibration results matched previous work on comparison

between homomorphic and heteromorphic methods [38]. The most problematic areas for homomorphic methods are steep slopes facing towards the radar, where the estimated illuminated area is both over- and underestimated. For these areas, a heteromorphic approach through DEM integration is more appropriate. The projection angle method coupled with resampling of the area to radar coordinates provides a significant improvement to the local incidence angle model and shows a much closer agreement with the heteromorphic results. The main factors to consider when choosing a calibration method are as follows:

- The UAVSAR sensor is electronically steered due to wind turbulence. Therefore, additional radiometric distortions are introduced by non-zero steering and aircraft pitch and yaw angles. For example, it was found that a steering angle of 8° introduced an additional 6 m^2 of illuminated area for the near range on flat terrain, which can lead to calibration errors on the order of 0.5 dB. These geometries are not readily corrected by the heteromorphic method since broadside viewing is usually assumed. On the other hand, the projection model automatically corrects for distortions due to those angles since they are incorporated into the look vector presented in Eq. 2.11.

- The quality of the heteromorphic correction is heavily dependent on the resolution of the DEM with respect to the radar backscatter image. As previously mentioned, the nominal pixel spacing of the DEM should be

$\leq 1/3$ the pixel spacing of the radar image. Integration of the oversampled DEM requires significantly more computational time than the homomorphic methods.

- The process of resampling the area image estimated from the projection angle often involves some form of averaging, which tends to cause a loss in resolution of the resultant area image in radar coordinates. Fine-scale features imaged by the radar may therefore be over- or under-corrected depending on the viewing geometry and the resampling procedure chosen. This effect was observed in the slight overestimation of area by the projection angle method coupled with an inverse distance weighted average.

2.2 Chapter Summary

An assessment of the performance of different radiometric calibration methods as applied to high resolution airborne radar backscatter data was presented. In general, the results matched previous work comparing homomorphic and heteromorphic corrections applied to satellite radar data. Homomorphic corrections applied in map geometry performed poorly for regions of high relief where both over- and underestimation of the illuminated area occurred. Qualitatively, this effect was easily observed in difference images between the homomorphic and heteromorphic methods, where the differences were most prominent on high slopes facing toward the radar. Performance of the homomorphic methods was significantly improved by using the projection angle and

resampling the illuminated area estimates to the radar coordinates to perform the correction in that geometry. For data acquired with low steering, pitch, and yaw angles, the heteromorphic facet model will provide the best calibration. Satellite data would be suitable for this calibration, where the altitude of the spacecraft and the assumed broadside viewing minimize any residual motion effects. For non-negligible Euler and steering angles, as is the case for most airborne data, the projection angle method will provide better correction in the near range of the image. Both methods would benefit from the use of a high resolution DEM to capture fine-scale features imaged by the radar. The impact of low DEM resolution on the calibration performance will be discussed in the next chapter.

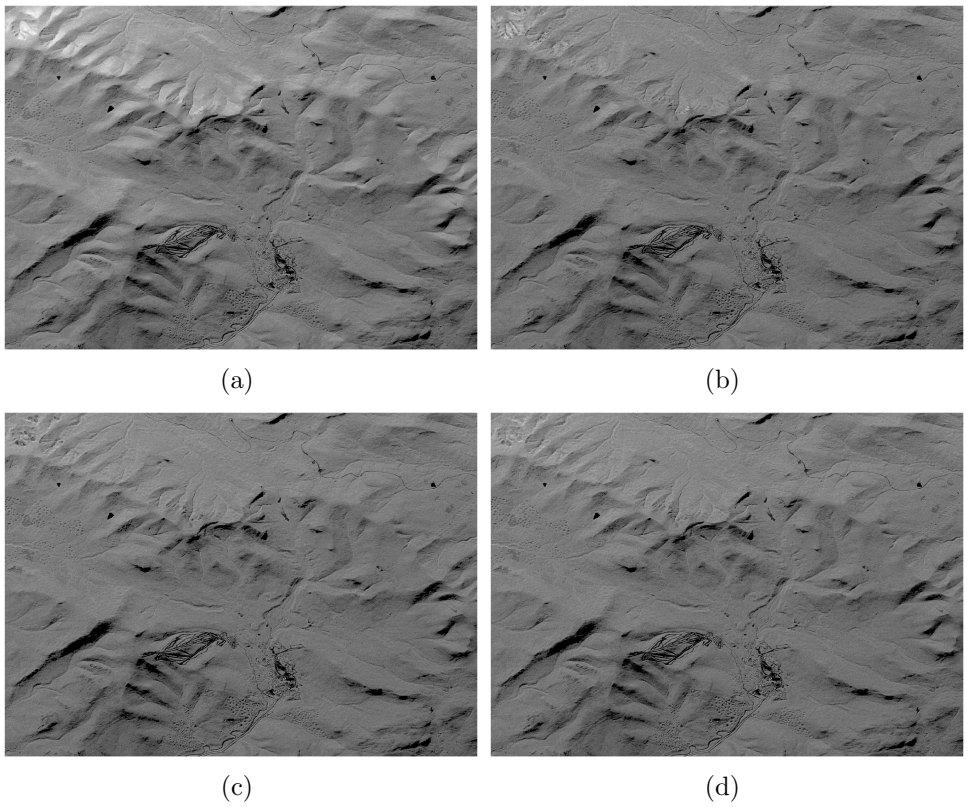

(a) (b)

(c) (d)

Figure 2.1: (a) Uncalibrated HVHV image over Bartlett Forest in the White Mountains in New Hampshire; Calibrated HVHV images using the local incidence angle method (b), the projection angle method (c), and the heteromorphic/facet method (d). Calibration is most significant on slopes facing towards the radar (bright regions), although the $\sin\theta_i$ correction is often insufficient.

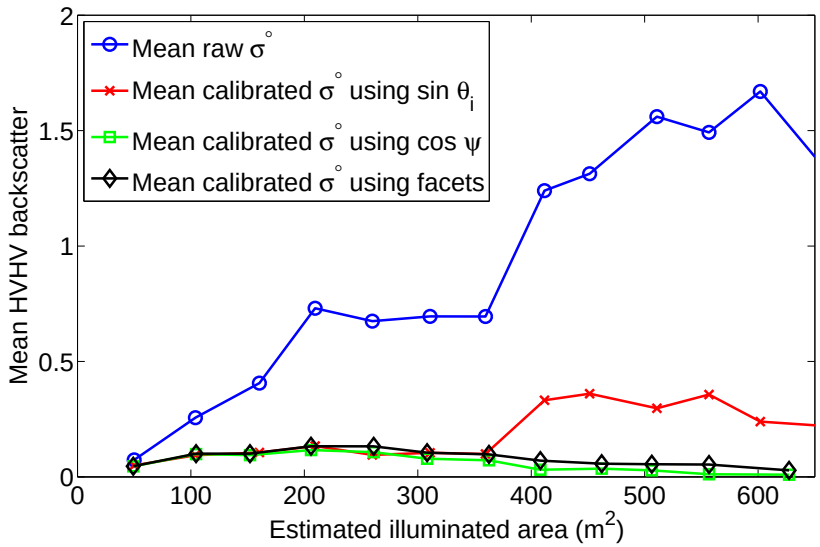

Figure 2.2: Mean HVHV backscatter vs. estimated illuminated area for different calibration methods

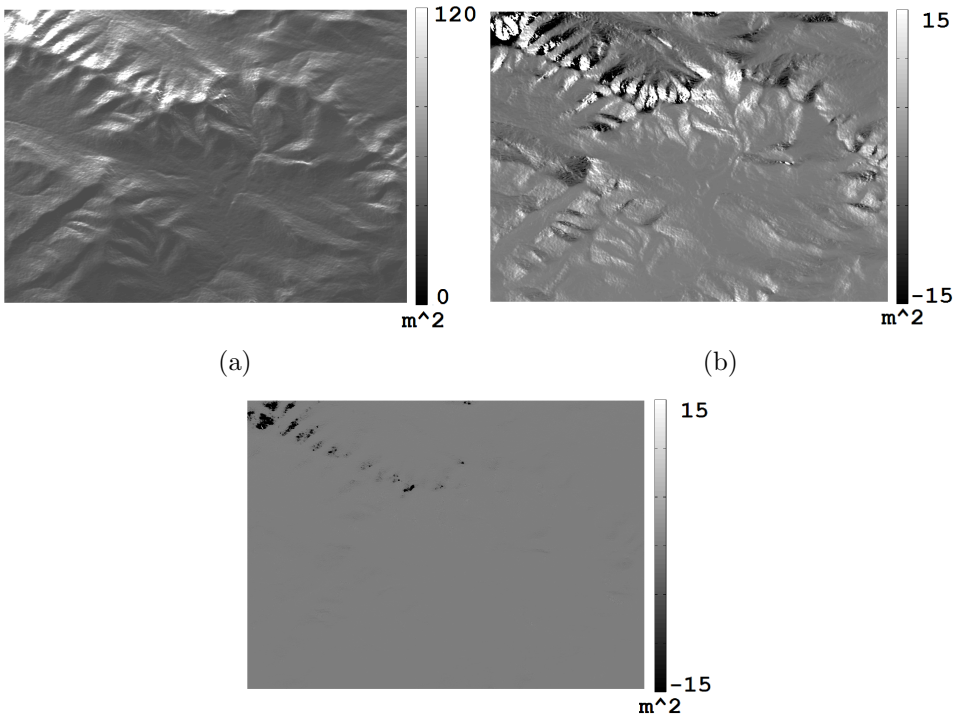

(a) (b)

(c)

Figure 2.3: (a) Estimated illuminated area using facet model; Difference in illuminated area between facet model and: local incidence angle model (b); projection angle model (c). There are significant differences between the facet and $\sin\theta_i$ predicted areas while $\cos\psi$ displays much closer results.

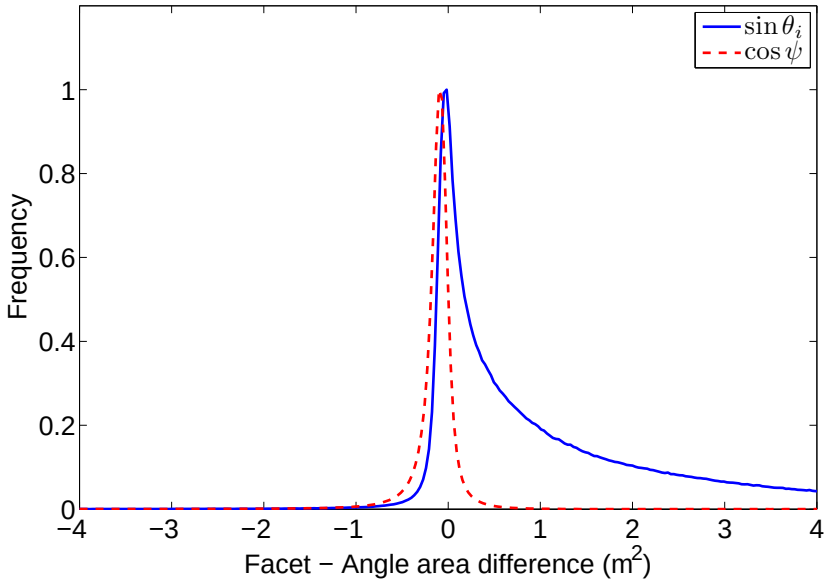

Figure 2.4: Histogram of differences in area estimates between heteromorphic (facet) and angular methods. Wide peak in $\sin\theta_i$ histogram indicates large distribution of errors while sharp, prominent peak in $\cos\psi$ histogram shows close agreement with the heteromorphic method.

Chapter 3

Estimation of Calibration Error due to DEM Resolution

An important aspect of using digital elevation models (DEMs) to perform radiometric calibration of radar images is to quantify DEM error and its impact on the calibration. Any DEM error will contribute to the variance already exhibited by the backscatter data and propagate to backscatter-derived physical quantities, e.g. aboveground biomass. For this work, the main focal point was to determine the amount of calibration error resulting from use of a low resolution DEM for calibrating high resolution radar data. Low resolution DEMs will fail to capture and correct fine scale topographic features that are imaged by the SAR sensor.

DEM error can be estimated either empirically or semi-empirically through the use of parametric models. Empirical methods are the most direct way to compute a DEM error for a given scene. These methods typically involve comparison of the DEM values with independent elevation measurements, such as GPS points [14]. However, the DEM error estimates are dependent on the quality of the ground truth data and can vary from scene to scene. A powerful semi-empirical method makes use of the Fourier transform

to characterize terrain [15].

Fourier transforms of terrain profiles result in the construction of "energy spectra", or power spectra [15], to characterize the undulations of topography to the DEM Nyquist wavelength, or twice the pixel size. Ideally, the terrain profiles should have as small a sample spacing as possible in order to fully characterize all fine scale features. High resolution airborne lidar data with resolutions of 1 m and elevation accuracies less than 10 cm provide a good balance between fine sample spacing and data storage size. Therefore, terrain power spectra computed using lidar data can be used as "truth" and compared to power spectra for coarser resolution DEMs. To estimate SRTM accuracy, terrain power spectra can be constructed over the full range of terrain classes, i.e. from high to low relief, enabling a database or look-up table of spectra parameters that can be readily consulted to estimate local error. The advantage of this method is its widespread applicability to DEMs of different scenes, coordinate systems, and data types.

In this section, Fourier transforms are performed on sufficiently sampled circular transects of airborne lidar data over three study sites. Power spectra are computed, and models relating the spectrum values to the spatial frequencies are derived and compared to spectra computed from SRTM DEMs over the same sites. The power spectra differences are used to estimate the error in terrain slope as calculated from the SRTM DEM. The error estimation is validated through a direct comparison with terrain slope derived from the lidar data. The error is then propagated to estimate backscatter calibration

error.

3.0.1 Study regions and DEM data

3.0.1.1 Lidar data

High resolution airborne lidar images were downloaded from NCALM (National Center for Airborne Laser Mapping) over three distinctly different study sites: 1) Silver Plume, CO; 2) Pleasant, ME; and 3) Plum Island, VA. The data were acquired using an Optech ALTM system and were filtered by NCALM to remove vegetation and buildings, leaving only the elevations due to bare earth. The data have a nominal vertical bias of 0.05 m with a scatter of 0.05 m (as compared to GPS data) [36]. The data were provided at a 1 m spacing in UTM, NAVD88 coordinates and were subsequently transformed to WGS-84, height above ellipsoid (HAE) coordinates with a 1/30-arcsecond pixel spacing (the 2003 geoid model was used to convert the NAVD88 heights to HAE). The study sites were chosen to be representative of steep/rough, moderate, and flat terrain, and have the terrain parameters presented in Tab. 3.1.

3.0.1.2 SRTM data

Since UAVSAR data are usually georegistered to SRTM DEMs, SRTM data was downloaded over the same study sites. DEM elevation values are geolocated on the WGS-84 ellipsoid and are orthometric relative to the Earth Gravitational Model 1996 (EGM96). The full gravitational model (spherical

harmonic coefficients to degree and order 360) was used to convert the EGM96 heights to HAE. Elevation data are provided in integer format with a precision of $\pm$ 1 m.

Several studies have been performed to assess the vertical accuracy of SRTM data. ICESat waveform lidar data was used by Carabajal and Harding [9] to measure the elevation error of SRTM values over areas of low relief and sparse vegetation, high relief and sparse vegetation, and low relief and dense vegetation. It was found that the greatest errors occurred over the high relief and sparse vegetation areas with elevation differences of -5.61 $\pm$ 15.68 m between ICESat and SRTM. It is expected that dense vegetation would introduce additional error since C-band radar tends to scatter off canopy tops. Rodríguez et. al. [33] used globally distributed GPS data and ground control points over both land and oceans to determine absolute geolocation, height, and relative height error for the main landmasses with average results of 9.8 m, 6.8 m, and 7.0 m, respectively.

In addition to vertical accuracy, studies seeking to determine the true horizontal resolution of SRTM data have been performed. Smith and Sandwell [39] and Pierce et. al. [30] used National Elevation Dataset (NED) DEMs and high-resolution airborne lidar data to perform a cross-spectral analysis with SRTM data. Specifically, the coherence, γ^2_{xy}, was calculated to measure the correlation between the SRTM data and the two reference elevation datasets, resulting in an estimate of the resolution at which the SRTM signal-to-noise ration (SNR) fell below 1. Results show a resolution between 30-60 m which

was attributed to the use of a lowpass boxcar filter being applied to the SRTM data to reduce noise.

3.0.2 Method

3.0.2.1 Fourier Analysis

Normal rectilinear profiles extracted from DEM data tend to have sharp cutoffs at the ends, i.e. large differences between the first and the last elevation values. This truncation can introduce a leakage effect and additional frequency components in the power spectrum [5]. Additionally, the profiles often have residual linear trends that are dependent on the direction that the transect is taken. These factors lead to power spectra that can vary significantly for sample areas within relatively close proximities to one another. Circular transects were used to extract elevation profiles that were periodic to eliminate leakage effects expected from normal rectilinear transects [5]. For each study site, multiple circular transects were extracted from the full resolution lidar DEMs, with each circle having a radius of $\approx$ 600 m. The Fourier transform was computed as follows:

$$X(k) = \sum_{j=1}^{N} x(j)\omega_N^{(j-1)(k-1)} \tag{3.1}$$

where $\omega_N = e^{(-2\pi i)/N}$, $X(k)$ is the Fourier component corresponding to the integer Fourier frequency k, $x(j)$ is the elevation value corresponding to transect position j, and N is the number of samples in the transect. The power

spectra values are computed as follows:

$$S(k) = \frac{2L}{N^2} |X(k)|^2 \tag{3.2}$$

where L is the length of the transect in meters. Since the transects are formed along a circle, the sinusoidal components computed through the Fourier transform correspond to sinusoids along the circle, rather than along a straight line through space. In other words, the spatial frequencies for the circular transects correspond to arclengths rather than Euclidean lengths for rectilinear transects. The length difference between the arclength and Euclidean length is predominant for the longer wavelengths where the straight line approximation for the arclength fails. Therefore, for the analysis, wavelengths longer than 1/10th of the circumference of the circle are discarded, allowing for a length difference no larger than 2% [5]. The spectra from the multiple transects were then averaged to obtain smoother estimates for the overall power spectra for each study site.

Before the Fourier analysis could be performed on the SRTM data, the DEMs were first oversampled to a 1/5-arcsecond spacing using bilinear interpolation to match the resolution of UAVSAR geocoded products. Then, similar circular transects were extracted, and an average power spectrum was computed for each site. Additionally, a best-fit line was fit to the data with the following form [15, 5]:

$$S = Ef^{\alpha} \tag{3.3}$$

which in log-log space would have the functional form of a straight line:

$$\log S = \log E + \alpha \log f \tag{3.4}$$

Fitting a function to the spectra allows for simpler parameterization of the spectra and facilitates DEM error prediction.

It is expected that the SRTM power spectrum, when compared to the associated lidar spectrum, will have very low Fourier components in the higher frequencies, particularly at the frequencies associated with pixel spacings smaller than the SRTM spacing of 1-arcsecond. Therefore, the difference in Fourier amplitudes should be a descriptor for the approximate DEM and slope/aspect error at that scale. Given a reference Fourier amplitude at a given frequency f_k, an amplitude loss (ΔX_k) can be computed. In this case, the reference amplitude is provided by the lidar spectrum, and the amplitude loss is the difference between the lidar Fourier amplitude and the SRTM Fourier amplitude at a particular frequency. To translate the amplitude loss to two-dimensional slope and aspect error, the derivatives of Eq.'s 2.2 and 2.3 can be derived as [43]:

$$dS = \frac{f_x df_x + f_y df_y}{(1 + \tan^2 S) \tan S} \tag{3.5}$$

$$dA = \frac{f_y df_x + f_x df_y}{\tan^2 S} \tag{3.6}$$

For the purpose of error prediction, it can be assumed that $f_x = f_y$ and $df_x = df_y$. Since the amplitude loss is calculated along the circular transect,

the one-dimensional gradient error df_x can be computed directly:

$$df_x = \frac{2\Delta X_k}{\lambda_k} \tag{3.7}$$

where λ_k is the wavelength. For this work, the focus was on analyzing the error expected at the UAVSAR pixel spacing of ≈ 6 m, which corresponds to a minimum recoverable wavelength of 12 m(i.e. Nyquist).

3.0.2.2 Direct DEM Comparison

In order to validate the error prediction method using the Fourier transform, the SRTM DEM and its derived topographic variables were compared to the lidar derived ground values. Since the topographic gradient differences were of primary interest when considering calibration error, the differences between the SRTM slope/aspect and the lidar slope/aspect were computed. However, it was found that the direct subtraction of the lidar and SRTM aspects is sensitive to mis-registration between the two datasets since the aspect values are modulo 2π. Aspect "differences" on the order of 2π were common and corrupted the statistics for the aspect comparison. By examining Eq.'s 3.5 and 3.6, it can be concluded that validation of the slope error prediction is sufficient for the corresponding aspect error predictions, so direct comparisons were constrained to terrain slope. Both datasets were co-registered and resampled to the UAVSAR pixel spacing of 1/5-arcseconds. The terrain slope was computed for both DEMs using Eq.'s 2.2 and 2.3. Once the slope images were generated for each study site, slope differences were computed along the same circular transects used for construction of the Fourier power spectra.

3.0.3 Results and Discussion

3.0.3.1 Terrain power spectra

In general, as the local relief of the site increases, the y-intercept of the linear fit of the power spectra in log-log space increases as seen in Fig. 3.1 and Tab. 3.2. The line-fit slope, α, also increases with local relief, although the increase is less pronounced. As expected, for all three sites, the SRTM spectra values are lower than the lidar values for most of the frequencies, meaning the SRTM DEMs are unable to fully capture the terrain undulations, particularly in the higher frequencies. In fact, the SRTM signature at the high frequencies should be very small since the DEM records no information at those spatial scales. The spectrum at these wavelengths is most likely distorted due to aliasing and the bilinear interpolation used for oversampling.

From previous studies on SRTM resolution [39, 30], the two power spectra were also expected to match at the frequency corresponding to a wavelength of 120 m, $\approx$ -2.08 in the log scale. While the Plum Island study site shows a crossing of the spectra at that wavelength, the other two study sites show similar but different values. This result may imply a few different factors: 1) the true resolution of the SRTM data over the other two sites may be greater than 60 m; 2) the spectra may be aliased in the higher frequencies due to oversampling; or 3) the vegetation patterns may be introducing further frequency distortions. To test these factors, an identical Fourier analysis was performed on lidar data that was first subsampled to 1-arcsecond and then oversampled to 1/5-arcsecond. This way, a bare earth simulation to the SRTM DEMs could

be obtained. The simulated SRTM power spectrum (Fig. 3.2) very closely matched the 1 m lidar spectrum to a wavelength of 60 m, as expected. On the other hand, the true SRTM spectrum differed from both for all wavelengths. Therefore, the most likely causes for the differences in the SRTM spectra at the lower frequencies are factors 1 and 3 listed above. Factor 3 can be expanded to include other SRTM elevation error sources, such as speckle noise and data precision.

3.0.3.2 Slope and aspect error prediction

Shaded relief maps formed using the high-resolution lidar data (Fig. 3.3a) allow for easy observation of the fine scale of topographic features that are captured by the elevation data. The slope difference between the lidar and SRTM (Fig. 3.3b) reveal that most of the differences arise along areas such as ridge lines and rivers, areas that the lower resolution of the SRTM data tend to average out. Such features often have spatial scales much smaller than 1-arcsecond. Nevertheless, the distribution of the slope differences appears to be concentrated on the higher frequency terrain undulations; very few low frequency/large spatial extent slope differences are evident in the image. This observation can be compared to the power spectra, where the lidar and SRTM spectra exhibit larger differences at the higher frequencies.

The slope and aspect RMSEs computed from the both the direct DEM comparison and the Fourier analysis show good agreement for all three sites (Table 3.3). The Fourier method started off with a slight overestimation of the

slope error for the steepest site and transitioned to a slight underestimation for the flattest site. However, this result may be more of a reflection on the direct DEM comparison, which is susceptible to geolocation errors and misregistration of the DEMs. The Fourier method is insensitive to such errors since the power spectra are computed for the whole region and are mainly invariant to the choice of reference system. The Fourier predicted aspect error increases with decreasing slope, which can be confirmed through inspection of Eq. 3.6.

To examine the impact of the slope and aspect errors on the overall calibration error, propagation of errors can be used on a suitable area estimation equation. First, the general radiometric calibration in decibels can be expressed as:

$$\sigma^{\circ}_{dB} = 10 \log_{10} \left(\beta \frac{A_{ref}}{Area} \right) \tag{3.8}$$

The area estimation error can be expressed with respect to errors in slope and aspect:

$$\Delta Area^2 = \left(\frac{\partial Area}{\partial S} \Delta S \right)^2 + \left(\frac{\partial Area}{\partial A} \Delta A \right)^2 \tag{3.9}$$

For this analysis, the area formula based on the projection angle was differentiated with respect to slope and aspect to compute the area error. The dB error in the calibration can then be expressed as:

$$d\sigma^{\circ}_{dB} = \frac{10 \Delta Area}{Area * \log 10} \tag{3.10}$$

The calibration error is most sensitive to slope errors when the surface aspect is equal to the azimuth angle of the sensor, i.e. when the surface normal is

oriented directly towards the sensor. In fact, the term $\frac{\partial Area}{\partial A}$ is eliminated under this condition. On the other hand, when the surface aspect is perpendicular to the sensor azimuth, the calibration error is most sensitive to aspect errors. Nevertheless, the sensitivity to slope errors outweighs the sensitivity to aspect errors.

To examine this sensitivity effect, the calibration error was computed for each site using the average slope and slope/aspect error estimates. Additionally, the contributions from the slope and aspect errors were isolated by computing the error for two cases: 1) $A = HEAD + \pi/2$, and 2) $A = HEAD$. For the Pleasant, ME and Plum Island, MA sites, the slope and aspect calibration errors are fairly equal and are both less than 0.5 dB (Fig. 3.4). Even though the aspect RMSE for the Plum Island site was significantly higher than the other two sites, the resultant aspect calibration error was still fairly minimal due to the low relief of the terrain. As terrain slope increases, both slope and aspect calibration error increase, although as seen by the slope calibration error for the Silver Plume, CO site, the increase in slope calibration error far exceeds the increase due to aspect error. This result is a combination of a decrease in aspect error and an increase in slope error with increasing terrain slope (see Tab. 3.3).

3.1 Chapter Summary

Calibration error for a given DEM was shown to be quantifiable through a comparison of the power spectrum for that DEM with a suitable lidar-derived

power spectrum. Thus, in order for this method to be used for an arbitrary study site, the terrain "class" for that site must be determined by an analysis of the local relief and the mean terrain slope for that area. Once a class is chosen, reference power spectrum parameters for that class can be determined and compared with the computed parameters for that DEM. The difference in spectrum values can be used to predict the calibration error for the DEM at a given wavelength. The advantages of this technique include the lack of a need for site specific ground truth, invariance to coordinate systems, relatively rapid calculation, and a demonstrated consistency between DEMs from different test sites. Future work will involve populating the spectra database with more terrain classes and using terrain data from other sources (e.g., other lidar data, high resolution photogrammetry, or ground measured transects) to eliminate any systematic effects from contaminating the spectra parameters.

Table 3.1: Terrain parameters for DEM study sites

Study Site	Acquisition Date	Local Relief	Mean Terrain Slope
Silver Plume, CO	9/30/2005	1300 m	26.3°
Pleasant, ME	10/31-11/11/2007	880 m	9.9°
Plum Island, MA	10/1/2005	15 m	1.9°

Table 3.2: Power spectrum line-fit parameters derived from lidar DEMs

Study Site	E	α
Silver Plume, CO	2.395×10^{-4}	-3.273
Pleasant, ME	3.421×10^{-5}	-3.336
Plum Island, MA	5.890×10^{-6}	-3.582

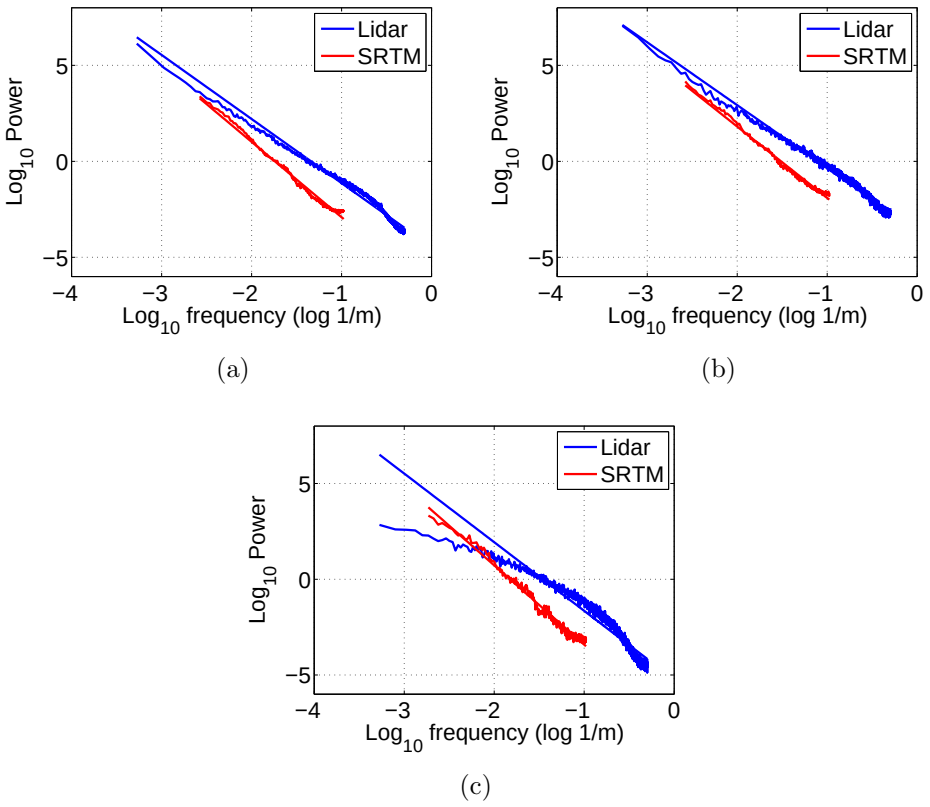

Figure 3.1: Average power spectra of study sites using multiple circular transects of lidar and SRTM DEMs. The study sites are Silver Plume, CO (a), Pleasant, ME (b), and Plum Island, MA (c). As mean slope and local relief increases, the spectra are shifted upwards in log-log space while the best-fit line slope remains similar. For all three sites, the SRTM power spectra are lower than the lidar spectra and exhibit greater differences in the higher frequencies.

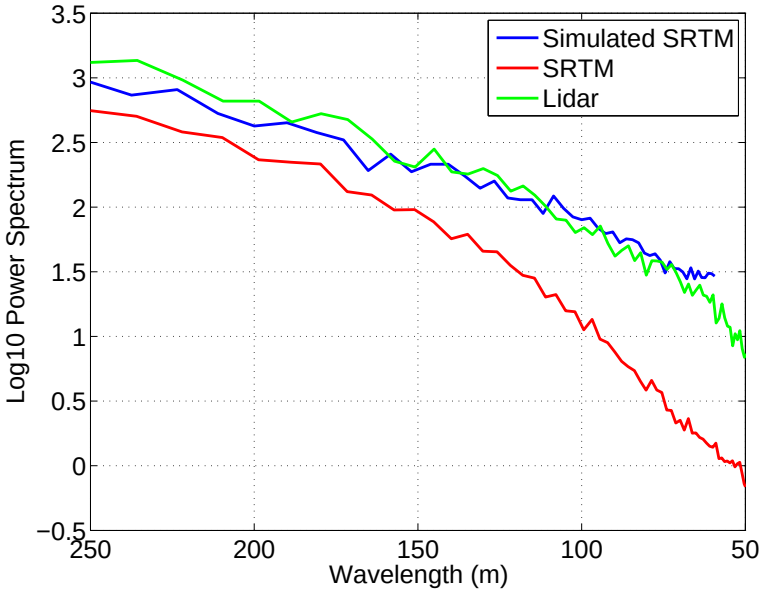

Figure 3.2: Power spectra over Pleasant, ME for SRTM and lidar DEMs and a simulated SRTM DEM formed from subsampled lidar data. The lidar and simulated SRTM spectra agree to a resolution of 60 m while the true SRTM spectrum differs from both for all wavelengths. This result suggests that either the native SRTM resolution or vegetation heights in the SRTM elevation values are causing the spectra differences rather than aliasing from oversampling.

Table 3.3: Predicted terrain slope error for three study sites

Study Site	(Lidar - SRTM) slope RMSE	Fourier predicted slope RMSE	Fourier predicted aspect RMSE
Silver Plume, CO	7.38°	8.14°	20.36°
Pleasant, ME	4.15°	4.17°	27.07°
Plum Island, MA	2.79°	2.42°	78.39°

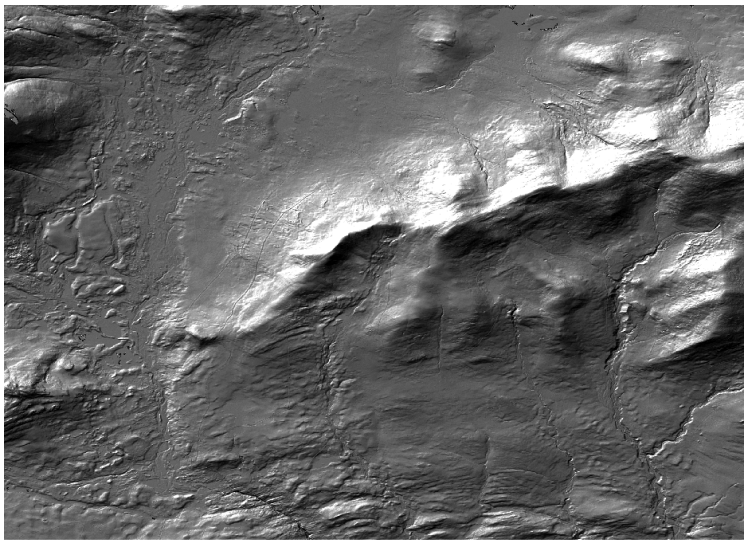

(a)

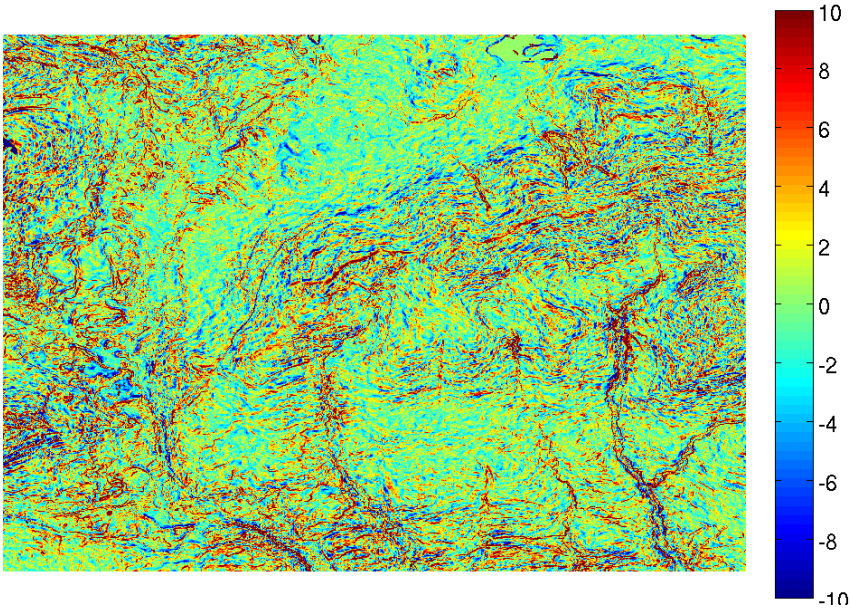

(b)

Figure 3.3: Pleasant, ME shaded relief (a) and slope differences between lidar and SRTM derived slope (b). Most differences arise from the fine-scale features that are not captured by the SRTM DEM due to its coarser resolution.

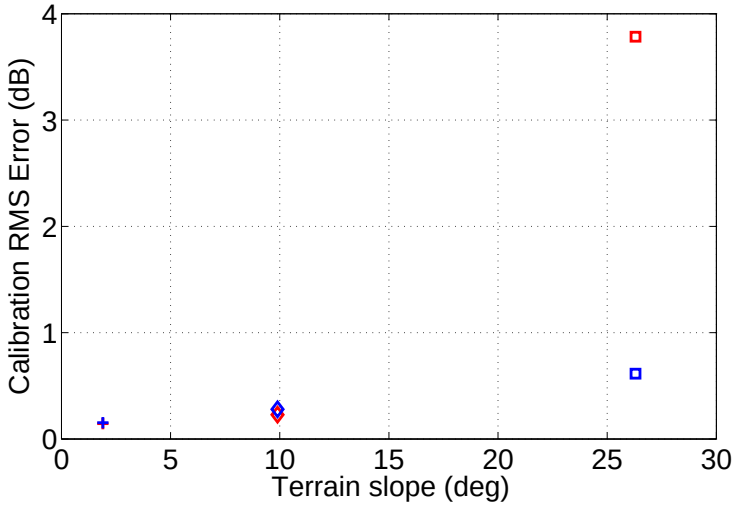

Figure 3.4: Predicted calibration error for three topographic study sites; '□' - Silver Plume, CO, '◇' - Pleasant, ME, '+' - Plum Island, MA. Slope effects are isolated by setting $A = HEAD + \pi/2$ while aspect effects are maximized with $A = HEAD$. Red markers indicate the slope dominant case while blue markers indicate aspect dominant case. For the Pleasant and Plum Island sites, the two error effects are fairly equal. However, for Silver Plume, the slope error is far more dominant than the aspect error.

Chapter 4

SAR Observation of Biomass

The main objective for remote sensing of forest ecosystems is to provide large spatial coverage at resolutions and time periods necessary for monitoring on regional and global scales, which is the most critical limiting factor for field collected forestry data. Much of the recent focus for forestry remote sensing has been on the quantification of biomass and ecosystem structure. Knowledge of such quantities allows for more thorough monitoring of carbon sources and sinks and the effects caused by land use change [22]. Currently, the most promising remote sensing technologies for this purpose are lidar and SAR.

Lidar directly measures the vertical structure of forest canopies using laser waveforms and has been shown to be very capable for predicting biomass variables [4]. Lidar instruments use the time-of-flight principle to measure the distance between the sensor and a particular target. Generally, a laser waveform pulse is emitted from the sensor. The outgoing pulse is reflected from the target, and the lidar instrument measures the distribution of the reflected waveform. Traditional discrete lidar systems employ a built in peak-finding algorithm in the hardware to measure the distances to a fixed number of "returns", or peaks, in the returned waveform. For forestry applications, the

first and last returns correspond to the top of the canopy and the ground, respectively. Other lidar systems digitize the full waveform to further enhance the characterization of geometrically complex targets [18]. The NASA lidar systems SLICER (Scanning Lidar Image of Canopies by Echo Recovery) and LVIS (Laser Vegetation Imaging System) both make use of the waveform technology to measure forest canopies [8]. Previous studies have used the SLICER instrument in conjunction with coincident field data to develop a single regression equation for aboveground biomass in the temperate deciduous, temperate coniferous, and boreal coniferous biomes [25]. It was found that the equation, which uses the mean canopy height (MCH), was able to explain 84% of the variance in aboveground biomass. A subsequent study applied the equation to LVIS data collected over the Bartlett Experimental Forest, which is located within the White Mountain National Forest in New Hampshire [4]. The height of median energy (HOME) for the waveform was also used to predict aboveground biomass. It was found that on the footprint level, the HOME metric was able to better predict aboveground biomass than the generalized equation using MCH [4].

SAR backscatter data, when used in conjunction with field data, has been shown to be effective in measuring biomass density on very large scales [27, 23, 35, 31, 40]. This is due to the physical relationship between radar backscatter and live stems, branches, and foliage [35]. Polarimetric SAR takes advantage of the polarized nature of SAR signals to obtain further information about vegetation backscattering. The most commonly used polarizations are

linear combinations, i.e. HH, HV, and VV, where, for example, HV stands for horizontal transmit (H) and vertical receive (V). Co-polarized signals, particularly HH, exhibit backscatter at higher biomass levels dominated by dihedral scattering, i.e. scattering from trunk-ground interactions, which is mainly controlled by the geometric and dielectric properties of the trunk and local surface. HV signals at longer wavelengths tend to scatter from lower primary stems and branches and are more influenced by forest type. Studies have found that the cross-polarized channel (HV) is the most sensitive to above-ground woody biomass [32, 27].

However, one of the main issues involved with using SAR data has been that the backscatter values at all polarizations saturate past a certain biomass level. In other words, once the biomass saturation level is reached, the SAR sensor loses sensitivity to increasing biomass levels [27]. This result makes SAR more useful for areas of forest regrowth characterized by lower biomass levels [28]. Early work on biomass retrieval made use of satellite-based sensors such as ERS-1, JERS-1, and SIR-C [27, 31]. These satellites generally operated at C-band (5.8 cm wavelength) or L-band (23.5 cm wavelength). It was found that the shorter wavelength for C-band radar resulted in backscatter mainly from forest canopies. Additionally, the biomass density at which the backscatter saturated was only around 20 Mg/ha, which would only be practical for discriminating between forested and nonforested areas [27]. On the other hand, longer wavelength signals tend to scatter from tree trunks and larger woody components, allowing estimation of biomass to a higher satu-

ration level (60 - 100 Mg/ha for L-band and 200 Mg/ha for P-band, 74 cm) [27, 32]. However, the longest wavelengths, particularly P-band, run into operability issues for spaceborne platforms due to factors like Faraday rotation [32]. Therefore, much of the recent research has been focused on developing biomass relationships with L-band backscatter data, which has a higher sensitivity to aboveground woody biomass than C-band and is more amenable to spaceborne operation than P-band.

One of the main prospects for future satellite missions designed to map biomass and landcover change is the NASA/JPL Deformation, Ecosystem Structure, and Dynamics of Ice (DESDynI) satellite. The sensors included in the satellite will be a fully polarimetric L-band SAR system configured for repeat-pass interferometry and a multi-beam lidar system [16]. The lidar system wll be used to measure the vertical structure of tree canopies, leading to biomass estimates from allometric equations parameterized by field data. The polarimetric SAR sensor will be able to upscale the lidar biomass estimates through both backscatter and interferometric methods, where the latter is achieved through the relationship between interferometric decorrelation and biomass. In short, one of the main objectives for the DESDynI science team is to determine if LIDAR and SAR data can be used together to provide consistent and accurate biomass estimation on global scales [11]. The current NASA requirement for biomass retrieval accuracy for the DESDynI mission is ± 10 Mg/ha [11]. An obvious test bed for the DESDynI mission is to use LVIS lidar data in conjunction with UAVSAR L-band data to attempt to es-

timate biomass. Both missions have similar data acquisition parameters, i.e. average aircraft altitude and coverage, and would provide researchers with various test sites to analyze the performance and accuracy of biomass estimation algorithms.

Still, the biomass estimation process can vary from region to region and is affected by non-homogeneous forests, incidence angle, and field data collection protocol [26, 29]. Most importantly, as discussed in the previous chapter, radiometric distortions in SAR backscatter data due to topography can significantly alter the estimated biomass. Backscatter distortions on the order of 1 dB can cause biomass estimation errors around 10-15 Mg/ha, which already exceeds the specified accuracy for the DESDynI mission. For slopes facing towards the radar, one can expect even higher backscatter variations ($\approx$5-7 dB). For those areas, any possibility for reasonably accurate biomass retrieval is lost. Therefore, SAR images of forested areas on steep/hilly terrain need to be calibrated for both area and incidence angle effects as discussed in the previous chapter.

This chapter first provides a review of the biomass estimation methods for both lidar and SAR data. The methods are then applied to LVIS (Laser Vegetation Imaging Sensor) lidar data and UAVSAR data covering the Bartlett Experimental Forest in New Hampshire. Radiometric calibration through area normalization is performed on the UAVSAR data, and the effect of the calibration on the performance of the biomass estimation is analyzed both qualitatively and quantitatively. Additionally, calibration errors are es-

timated using a Fourier analysis of the reference DEM and are propagated to biomass estimation error using propagation of uncertainty principles.

4.1 Methodology

4.1.1 Study Area

The White Mountain National Forest is located along the White Mountain range in New Hampshire and is characterized by its population of eastern conifers and hardwoods. Located within the national forest is the Bartlett Experimental Forest, an area roughly 2,600 acres in size that has been managed since 1931. According to the USDA Forest Service, the main species of trees that can be found within Bartlett are sugar maple, spruce and fir in the higher elevations, hemlock, and white pine. Elevations range from 680 to 3000 ft with the majority of the aspects aligning with the north and east directions. The Forest Service has established 500 permanent 0.1-ha plots spaced roughly 200 by 100 meters apart and has cut about 55% of the forest area for experimental purposes. The remaining 45% of the forest has been untouched since 1890. Various field data metrics for the permanent plots have been acquired throughout the years with the most recent data set acquired in 2001-2003 [2].

4.1.2 Remote sensing data

LVIS LIDAR data was acquired over Bartlett on September 26, 1999 and July 18-26, 2003 [8]. For this study, the 2003 data set was used since previous work [4] found that the 1999 data was biased towards canopy height

underestimation when compared with field data. The 2003 LVIS swath covers approximately 8 $\times$ 60 km with a nominal footprint radius of 10 m and a footprint geolocation accuracy of 1-2 m. The data was delivered with the following information for each footprint: 1) time of acquisition, 2) latitude/longitude, 3) ground elevation above reference ellipsoid, and 4) relative heights (RH) where 25, 50, 75, and 100% of the waveform energy occurs. The RH100 metric is analagous to MCH while RH50 is analagous to HOME. The ground elevations were gridded to 1/2-arcsecond spacing using a continuous curvature surface gridding algorithm included in the Generic Mapping Tools (GMT) software. The output map projection is geographic WGS-84. The RH50 points were gridded to the same pixel spacing using a nearest neighbor gridding alogorithm.

Multiple UAVSAR fully polarimetric L-band (1.257 GHz, 80 MHz bandwidth) SAR data were acquired over Bartlett on August 5, 7, and 14 in 2009. For each day of surveying, the flightline was flown at two different headings (71 and 250 degrees). Each swath covered an area of approximately 20 km in the range direction and 100 km in the azimuth direction. Incidence angles range from approximately 25° to 65°. The UAVSAR data encompasses nearly all of the area covered by the LVIS data. UAVSAR intensity images are delivered as multilooked complex products of the SLC data (3 range looks, 12 azimuth looks), where HHHH products correspond to $S_{HH}S_{HH}^{*}$ and are real valued while HHVV products correspond to $S_{HH}S_{VV}^{*}$ and are complex valued. The images are delivered in slant range and geographic map coordinates, where the slant range images were georegistered to a reference DEM [3]. The slant

range image pixel spacing is 4.9965 and 7.2 m in the range and azimuth directions, respectively, while the reference DEM (SRTM) was oversampled to a pixel spacing of 1/5-arcseconds. The data were calibrated by JPL for antenna pattern, cross talk, and projected ellipsoid area.

The August 5, 250 degree heading UAVSAR polarized intensity images (HHHH, HVHV, VVVV) were radiometrically corrected for topography using the projection angle algorithm presented in the previous chapter. The SRTM DEM delivered with the data was used to perform the radiometric correction in the slant range plane. The corrected images were then georegistered to the SRTM DEM using the SCH transformation with a registration error of less than 5 m. A false color RGB image (R - HH, G - HV, B - VV) can be compared with multispectral optical images to differentiate between ground target types (Fig. 4.1). For example, darker green areas, corresponding to stronger HV backscatter values, are mostly populated with coniferous trees and are predominantly at higher elevations. Strong surface scattering is observed over purple areas due to the dominance of co-polarized returns.

4.1.3 Predicted biomass relationships

Research by Lefsky et al. [25] used SLICER waveforms to relate MCH to field measured aboveground biomass for 25 $\times$ 25 m plots located within three distinct biomes (temperate deciduous, temperate coniferous, and boreal coniferous). The resulting equation has the form:

$$B = 0.378 * MCH^2$$

Anderson et. al. [4] performed a similar regression analysis using LVIS data over Bartlett (the same LVIS data used in this study). The HOME waveform metric was found to have better correlation with biomass than the MCH metric, both on the footprint level (0.07 ha) and the plot level (1 ha). The equation relating biomass to RH50 was the following:

$$B = 29.954 + 14.297 * RH50 \tag{4.1}$$

When applied on the footprint level, the resulting biomass prediction RMSE for the RH50 method was 58.03 Mg/ha while the MCH method resulted in an RMSE of 64.41 Mg/ha. For the plot level analysis, the RH50 method had an RMSE of 56.51 Mg/ha while the MCH method resulted in an RMSE of 63.27 Mg/ha. Both spatial scales showed improved relationships when special conditions were considered, i.e. using only relatively unmanaged plots and restricting areas of study to those mainly populated by coniferous trees [4].

Since LVIS data was the focus of this study, the RH50 method was used to predict aboveground biomass. Additionally, simulated infrared optical imagery formed from Landsat TM data was used to stratify the LVIS data into coniferous and deciduous classes. Then, RH50 grid points located within a 3 or 4 pixel square window were selected and averaged to constitute an estimation for RH50 on the plot level. 118 of these plots were chosen from coniferous regions and Eq. 4.1 was used to predict biomass for those plots. The maximum biomass was thresholded at 250 Mg/ha, i.e. any grid point with a biomass greater than the threshold was just assigned the threshold value for

the purpose of comparison to the UAVSAR predicted biomass (the actual range of estimated biomass was 10 to 380 Mg/ha). The biomass map (Fig. 4.2) can be compared to Fig. 4.1, and many common patterns can be distinguished between the two images. In particular, the coniferous higher elevation areas are characterized by lower biomass values while the deciduous/mixed forests have significantly higher values.

Research on biomass retrieval from SAR backscatter data has typically attempted to model the saturation of the backscatter values at high biomass levels with sigmoid functions, which are based on radiative transfer modeling of backscatter from forest canopies [27, 26]. The general model relating backscatter to biomass is then:

$$\sigma^0 = \alpha * \left(1 - e^{-\beta B}\right) \tag{4.2}$$

where α is a scaling constant, β is a constant to model attenuation of the radar signal through the forest, B is the biomass, and σ is the backscatter on a linear scale. Work from Saatchi et. al. [35] and Rignot et. al. [32] modified the sigmoid function to include backscatter contributions from multiple polarizations. Biomass is replaced by the natural logarithm, $\log(B)$, and the linear backscatter is converted to dB to obtain the following semi-empirical form:

$$\begin{aligned}\log(B) = a_0 + a_1\sigma^0_{HV} + a_2\left(\sigma^0_{HV}\right)^2 + b_1\sigma^0_{HH} \\ + b_2\left(\sigma^0_{HH}\right)^2 + c_1\sigma^0_{VV} + c_2\left(\sigma^0_{VV}\right)^2\end{aligned} \tag{4.3}$$

Both functional forms (sigmoid and quadratic) model the backscatter to biomass relationship as a nearly linear rise that reaches a saturation point at a certain

biomass level. The sigmoid function is generally suited for a single polarization of SAR data whereas the quadratic form takes all three polarizations into account. Since UAVSAR data is fully polarized, the quadratic form was chosen for this study. The objective is then to solve for the values of the constants that provide the best fit of the observed backscatter and aboveground biomass, which is usually derived from field measurements and allometric equations relating various tree parameters (height, diameter at breast height) to biomass. As a concept test for the DESDynI mission, LVIS-derived biomass was used as ground truth for estimating the parameters in Eq. 4.3.

4.1.4 Error analysis and propagation

While the radiometric calibration removes backscatter distortions due to topography, it also introduces additional variance to the backscatter data due to the variance of the DEM and DEM errors. The previous chapter introduced a method to estimate calibration error variance for a given DEM using a Fourier analysis of the terrain data. To apply that method to the Bartlett data set, the SRTM DEM had to be classified under a certain topographic class, i.e. a suitable reference power spectrum had to be chosen that matched the characteristics of the Bartlett topography. Using the SRTM DEM, the mean slope for the data set was determined to be 10.01°, which is very close to the mean slope of the Pleasant, ME site from the previous chapter. Furthermore, the relative proximity of the Bartlett forest to Pleasant justifies the use of the Pleasant power spectrum as a reference spectrum. Multiple circu-

lar transects were extracted from the Bartlett SRTM DEM, and an average power spectrum was computed. The power spectrum was compared to the Pleasant power spectrum to estimate terrain slope and aspect errors. These errors were then propagated to an overall calibration error. Once the calibration errors were computed, propagation of errors was used to predict the total biomass estimation error. From Eq. 4.3, partial derivatives with respect to each polarization lead to an expression for the biomass error:

$$\Delta B^2 = \left(\frac{\partial B}{\partial \sigma^0_{HV}}\right)^2 + \left(\frac{\partial B}{\partial \sigma^0_{HH}}\right)^2 + \left(\frac{\partial B}{\partial \sigma^0_{VV}}\right)^2$$

$$\Delta B = B\sqrt{\begin{array}{l}\left[\Delta\sigma^0_{HV}(a_1 + 2a_2\sigma^0_{HV})\right]^2 + \left[\Delta\sigma^0_{HH}(b_1 + 2b_2\sigma^0_{HH})\right]^2 \\ + \left[\Delta\sigma^0_{VV}(c_1 + 2c_2\sigma^0_{VV})\right]^2\end{array}} \tag{4.4}$$

The quantities $\Delta\sigma^0_{HH}$, $\Delta\sigma^0_{HV}$, and $\Delta\sigma^0_{VV}$ are equivalent since the calibration is applied equally for all polarizations. From the equation, it can be seen that biomass error is dependent on biomass itself. Areas with higher biomass will have greater errors.

4.2 Results and Discussion

Backscatter vs. biomass plots for the three linear polarizations show a distinct increase in backscatter with biomass until a saturation point of approximately 100 Mg/ha (Fig. 4.3). The HV backscatter had the highest correlation with biomass while the VV polarization had the lowest correlation. In terms of polynomial parameters, the HH and HV coefficients were fairly

similar. For all polarizations, the radiometric calibration had minimal effect on parameters of the polynomial fit (Tab. 4.1); figure 4.3 shows polynomial fits that are nearly identical for uncalibrated and calibrated data. Therefore, the scattering characteristics of the ground targets are nearly unaffected. However, calibration of the SAR backscatter did result in increased R^2 values. This result indicates that area calibration of the SAR data helps to reduce the overall variance, even when the variance due to DEM errors is ingested. It should be reiterated that there is still a significant dependence on backscatter with incidence angle that is not removed with the area calibration. In fact, when a simple gamma correction was applied, i.e. dividing the area calibrated backscatter by $\cos\theta_i$, it was found that the R^2 values increased to 0.57, 0.62, and 0.43 for HH, HV, and VV, respectively. The gamma correction also resulted in significantly different polynomial parameters, thus removing most of the dependence of the backscatter on incidence angle. It should also be noted that these results may be further influenced by the spatial distribution of the selected plots, i.e. how many plots were located in shadow vs. how many were on brighter regions sloped towards the radar. Generally, the plots were chosen on moderate hills where shadow and layover influences were minimal, thereby minimizing the overall effect of the area calibration. Additionally, the lower biomass values were selected from relatively flat areas where the forest had been cleared.

A comparison between UAVSAR predicted biomass computed from Eq. 4.3 and the "true" biomass computed from the LVIS RH50 height metric shows

that UAVSAR tended to overestimate the biomass values until the saturation point, where increases in LVIS-measured biomass resulted in the same predicted value for UAVSAR (Fig. 4.4). Similar to the biomass vs. backscatter results, the area calibration had a minimal effect on the biomass regression fit (Table 4.2). The resultant RMSEs and the parameters themselves are very similar (Note: the RMSE calculation assumes no error for the LVIS data).

The resultant biomass map of the subset area, where a threshold of 250 Mg/ha was enforced for comparison purposes with the LVIS biomass map in Fig. 4.2, shows that topographic effects are still noticeable where slopes facing towards the radar have "higher" biomass while slopes facing away have seemingly lower biomass (Fig. 4.5a). This behavior is largely due to the uncorrected dependence of backscatter on incidence angle and does not represent the true biomass distribution. Additionally, SAR speckle noise is evident in the image, and heavier filters are required to generate smoother biomass distributions. Comparison of Fig. 4.5a with Fig. 4.2 reveals some similarities, namely areas of lower biomass associated with coniferous trees. However, detection of higher biomass regions (>150 Mg/ha) that are clearly evident in the LVIS image was severely hampered by the saturation of the SAR data, leading to an overabundant distribution of moderate biomass regions (100-150 Mg/ha) throughout the UAVSAR map.

The computed biomass error due to calibration errors expected from DEM slope and aspect errors has an obvious range dependency: pixels in the near range can be expected to have greater errors than pixels in the far range

(Fig. 4.5b). Additionally, slopes facing towards the radar will have higher biomass uncertainties, which comes from a combination of two effects: 1) due to the insufficient calibration, foreslopes show higher "biomass" values, leading to higher biomass error from Eq. 4.4, and 2) simulation of the error equations for a range of slope and aspect angles show maximum error for foreslopes with aspects aligned with the azimuth of the sensor, i.e. local incidence angles approaching zero. Therefore, biomass estimation is highly sensitive in steep terrain and requires very accurate radiometric calibration.

4.3 Chapter Summary

This chapter provided a framework for assessing the impact of radiometric calibration on the biomass retrieval capabilities of L-band UAVSAR data. Specifically, radiometric distortions resulting from variations in the illuminated area were calibrated using the projection angle method presented in the previous chapter. Additionally, the suitability of large footprint LVIS data as a proxy for "ground truth" biomass was tested using previously established allometric equations for the RH50 metric. Combination of the LVIS data with the UAVSAR data for biomass retrieval provides an important testbed for the future DESDynI mission. The study site over the Bartlett Experimental Forest in New Hampshire was chosen due to its moderate relief in order to test the effectiveness of the calibration method over densely forested terrain. The results show that even for uncalibrated data, the backscatter show a general increase with LVIS predicted biomass up to a reasonable saturation point for

all polarizations. Calibration of the backscatter data for area effects from topography resulted in regression fits with higher R^2 values (a general increase of 0.07-0.08 R^2) but little effect on the regression parameters. These results largely ignore other error sources associated with SAR data, such as speckle noise, geolocation errors, and ground and canopy moisture causing changes in dielectric properties [35]. Therefore, the focus should be on the relative change in R^2 values between the uncalibrated and calibrated cases rather than the total R^2.

Calibration error due to DEM resolution was included in the analysis by using the Fourier based method presented in the previous chapter to predict slope and aspect errors. Then, the impact of the calibration error was propagated to predict biomass error. Since the calibration error is dependent on the slope and aspect of the ground, a biomass error map was produced indicating the areas where biomass retrieval tends to have the greatest difficulty. These areas were found to be on ground slopes facing towards the radar, and for the densely forested Bartlett site, the resultant biomass errors can reach upwards of 50 Mg/ha. These errors far exceed the planned DESDynI requirement of 10 Mg/ha and suggest that DEMs with greater resolution are needed to bring the calibration errors down. While correcting the backscatter for incidence angle effects does provide noticeable improvement, the correction is usually site specific and would require greater consideration of the range of tree species. One approach would be to use the LVIS ground points to perform the correction for the regions covered by both UAVSAR and LVIS data. The ground points

can be converted to a DEM with a higher native resolution than the SRTM DEM, leading to lower slope and aspect errors. This approach was actually tested and shown to improve calibration results. However, the DEM displayed artifacts from non-ground points, a result stemming from the high canopy density weakening the returned ground signal. This caused the roughness of the DEM to increase, causing increased variance of the area estimates. Therefore, further filtering of the ground points would be required to use this technique.

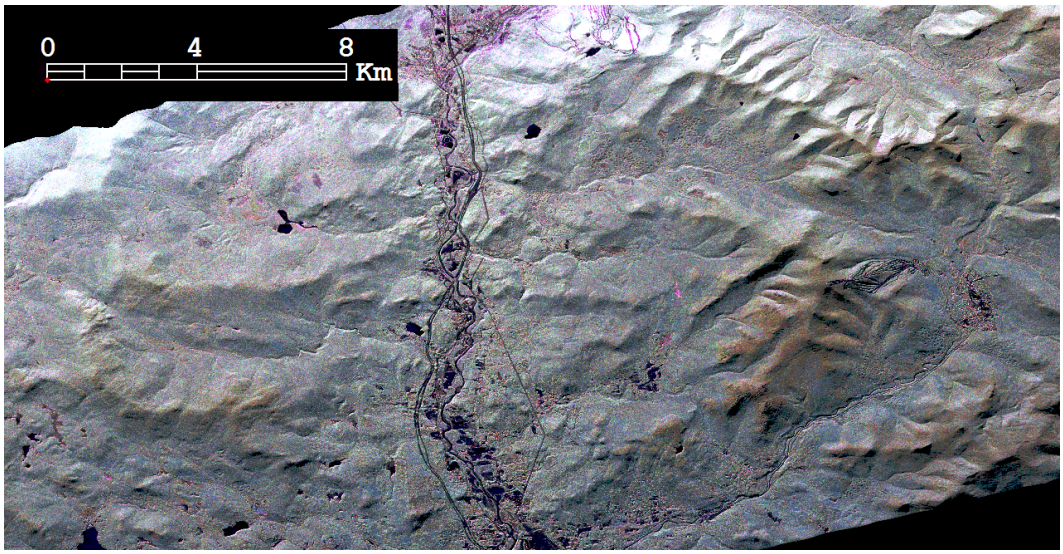

Figure 4.1: UAVSAR false color RGP map of the Bartlett Experimental Forest in NH

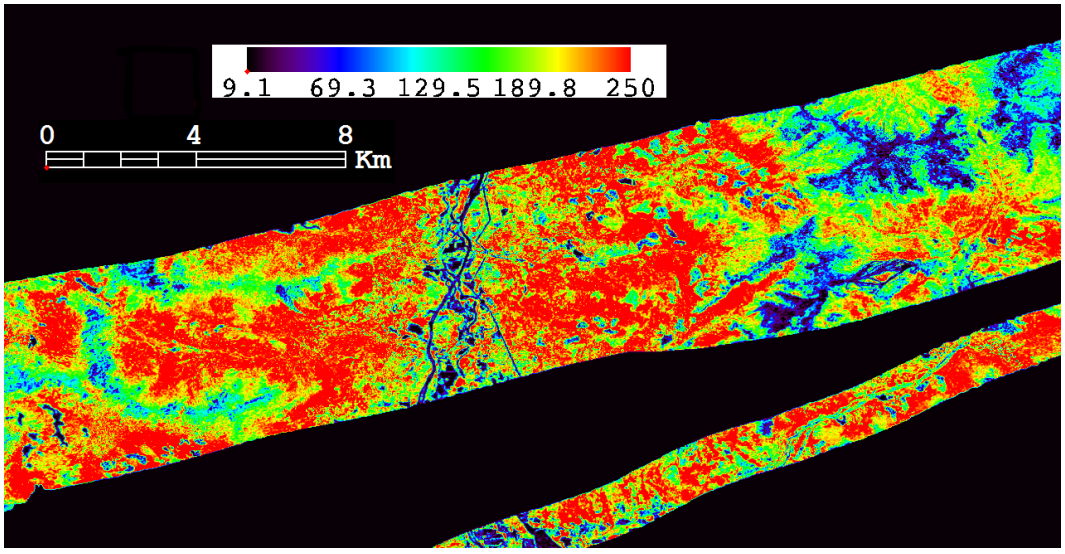

Figure 4.2: LVIS derived biomass map using RH50 metric

Table 4.1: Polynomial parameters for backscatter vs. biomass data

Coefficient	HH		HV		VV	
	β^0	σ^0	β^0	σ^0	β^0	σ^0
p_0	-111.48	-115.72	-130.61	-135.25	-51.93	-56.69
p_1	41.54	43.33	46.87	48.82	16.15	18.15
p_2	-4.15	-4.34	-4.67	-4.88	-1.53	-1.74
R^2	0.33	0.41	0.41	0.48	0.19	0.26

Table 4.2: Biomass regression parameters

	Parameter							
	a_0	a_1	a_2	b_1	b_2	c_1	c_2	RMSE (Mg/ha)
β_0	10.053	0.983	0.019	-0.558	-0.020	-0.119	0.004	50.8
σ_0	11.121	1.079	0.022	-0.631	-0.025	-0.004	0.009	50.3

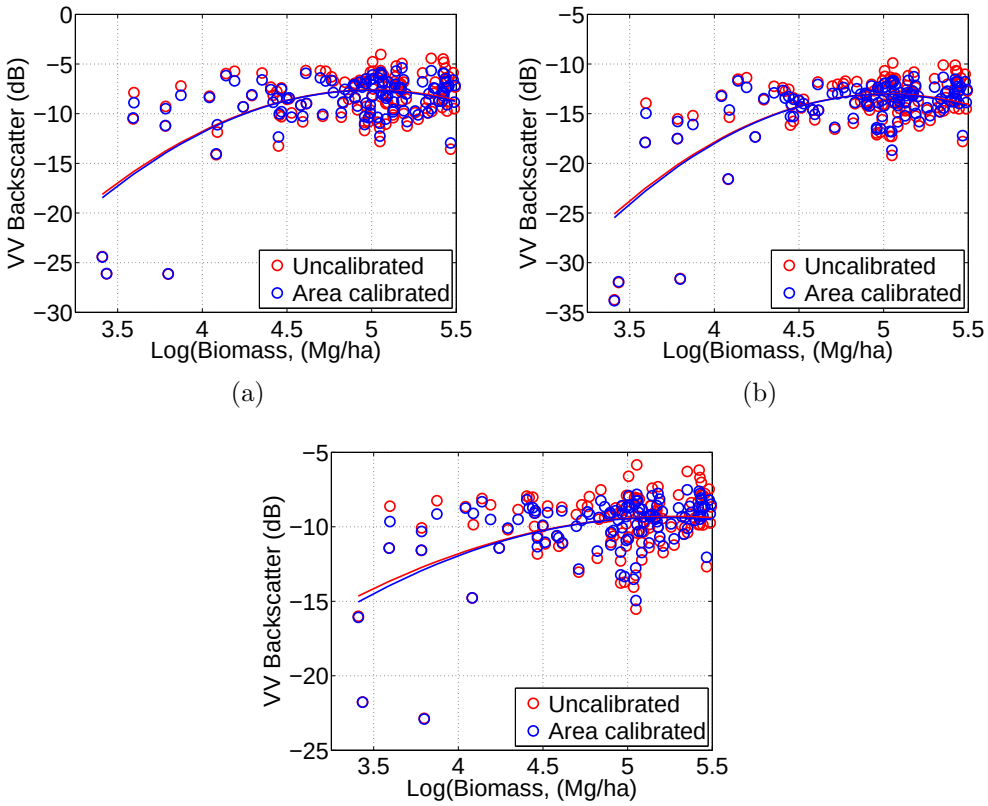

Figure 4.3: Backscattering coefficients vs. LVIS predicted aboveground biomass for the UAVSAR HH (a), HV (b), VV (c) linear polarizations. Data were averaged to the plot level (1 ha), and a quadratic function was fit to the data points. Calibration of the SAR data resulted in quadratic fits that were very similar to the fits obtained from the raw data, although the data scatter was reduced.

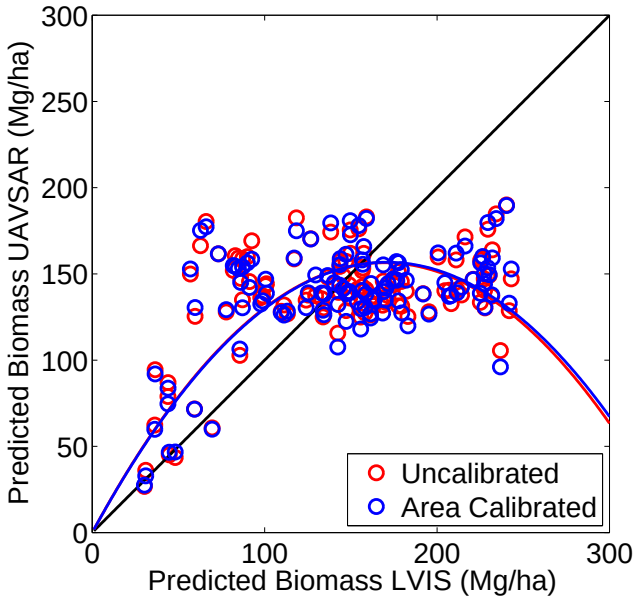

Figure 4.4: LVIS predicted vs. UAVSAR predicted biomass

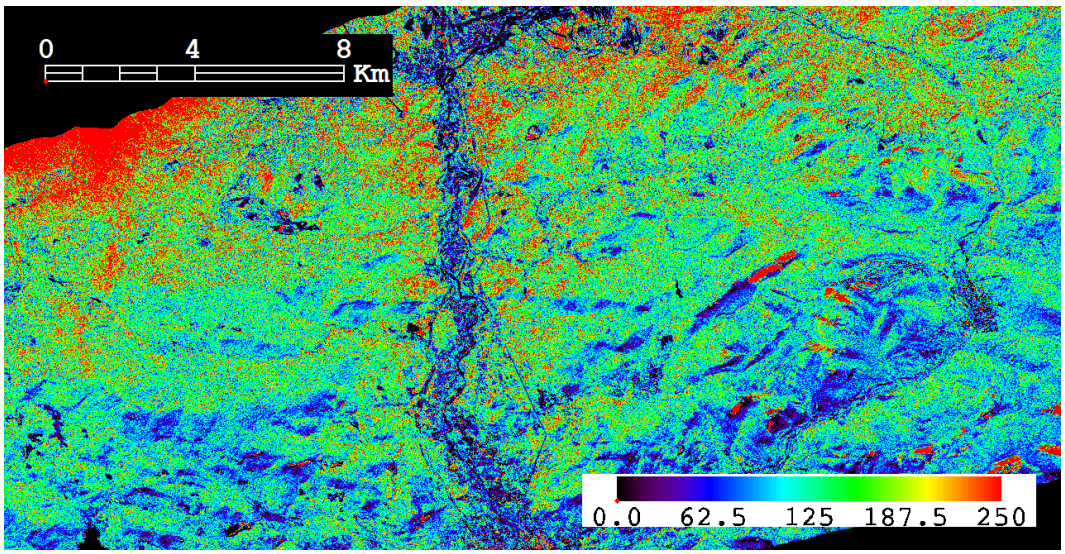

(a)

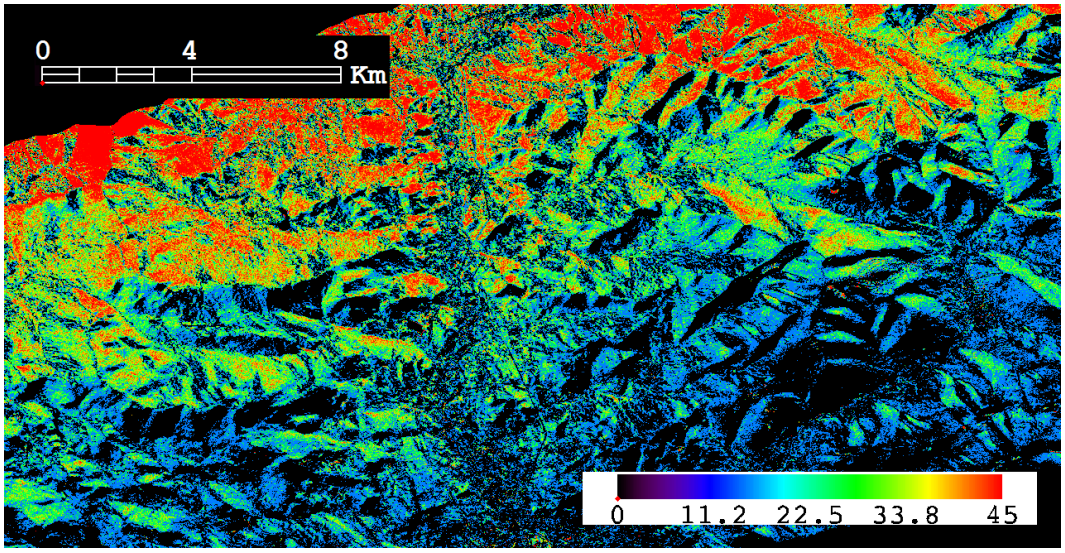

(b)

Figure 4.5: Bartlett biomass (a) and biomass error map (b). Note higher values for both biomass and biomass error on the foreslopes, where the latter is influenced by both higher biomass values and greater calibration error

Chapter 5

Conclusion

5.1 Research Summary

SAR backscatter data has the potential to retrieve aboveground biomass on a global scale. The longer radar wavelength and its proven operability on spaceborne platforms allows SAR to be an all-weather, daylight-independent imaging system and is well suited to map all types of vegetation. Furthermore, the high resolution of SAR systems would allow for the formation of global vegetation maps with unprecedented detail. The biomass estimation process involves fitting functional forms to backscatter vs. ground truth biomass. The DESDynI mission, in addition to an L-band polarimetric SAR sensor, will include a large footprint lidar system to measure the vertical canopy structure and canopy height. Studies have shown that extrapolating the lidar measured canopy height to biomass through allometric equations can provide reasonably accurate spatial estimates of biomass. Therefore, use of a spaceborne SAR system in conjunction with a lidar system would allow for global estimation of biomass that would be largely independent of field and in situ data, which tends to be costly and time consuming.

However, there are many obstacles and error sources involved with us-

ing SAR backscatter data for biomass retrieval. Speckle noise, geolocation errors, ground and canopy moisture effects, and radiometric distortions due to topography all complicate the estimation process and can vary from region to region. Topographic variations are the largest error sources and can be mitigated through absolute radiometric calibration. This paper presented a method to calibrate backscatter values for topography by normalizing the intensity values by the varying illuminated area. Several different techniques for modeling the illuminated area through knowledge of terrain height were presented, and their advantages and disadvantages were weighed. Pure homomorphic calibration is the simplest to implement and performs reasonably well for flat terrain. Heteromorphic calibration methods are more computationally intensive but perform significantly better for steep terrain. The most flexible approach is a combination of the two types, which was presented in this paper as the projection angle method with the area estimates mapped to radar coordinates. Using the projection angle allowed for the incorporation of aircraft residual motion effects from non-zero Euler and electronic steering angles, which are not taken into account during the DEM integration phase of heteromorphic corrections. Mapping the projection angle area estimates to radar coordinates increased the accuracy of the modeling for steep terrain, the most serious shortcoming of incidence angle based homomorphic corrections.

The calibration process itself is also subject to inherent error sources, mainly from the DEM used to estimate the illuminated area and associated projection and incidence angles. The DEM error source focused on here was

error due to low spatial resolution as compared to the resolution of the SAR image to be calibrated. As a test case, the calibration error expected from using a 1-arcsecond SRTM DEM to calibrate 1/5-arcsecond UAVSAR images was analyzed. Traditionally, DEM error can be estimated through comparison with ground truth, such as GPS or high resolution lidar data. Still, as with biomass ground truth, such validation data can be site specific, costly, and would not have the coverage necessary to validate DEMs from all regions. Therefore, a method was presented here to estimate DEM error for various terrain types without the need for widespread ground truth. The method revolved around Fourier transforms of circular profiles extracted from both low resolution SRTM DEMs and high resolution airborne lidar DEMs. The lidar power spectrum served as the reference, or "ground truth", spectrum due to the proven accuracy (<10 cm vertical) and spatial resolution (1 m) of lidar data. Both spectra were then modeled with linear fits in the log-log scale, resulting in coefficients for line slope (α) and intercept (E). Comparison of the power spectra for common sites revealed lower power spectra values for the SRTM data than the lidar data at shorter wavelengths, indicating a loss of topographic information at those wavelengths. For a particular wavelength, the spectrum difference allows for calculation of the slope and aspect error and the associated calibration error. This process was performed for flat, moderate, and steep terrain that had both lidar and SRTM data to perform the power spectra comparison, and the predicted errors were compared to the actual errors calculated through a direct comparison between the lidar and SRTM

DEMs. The error values matched up well and signify that this process can be applied to any SRTM DEM compared to the appropriate reference spectrum values.

Finally, the biomass estimation capabilities of L-band UAVSAR data were tested by using LVIS large footprint lidar data as a proxy for ground truth biomass and fitting second-order polynomials to the backscatter data. This approach is a good testbed for the DESDynI mission since the UAVSAR and LVIS platforms share common flight acquisition parameters and similar coverages. The UAVSAR images were radiometrically calibrated for topography using the projection angle method in order to quantify the effect of calibration on the biomass estimation process. It was found that both the uncalibrated and calibrated data were positively correlated with the LVIS biomass up to a saturation point, a behavior that is well documented for SAR data at high biomass sites. The calibration improved the R^2 values of the second-order polynomials fit to the backscatter data, but did not significantly alter the polynomial coefficients. The Fourier method for computing calibration error was applied to the SRTM DEM used for calibration, and the errors were propagated to biomass estimation errors. The spatial distribution of the errors showed greater errors for slopes in the near range and facing towards the sensor, a result due largely to insufficient calibration of those foreslopes.

5.2 Future Work

The radiometric calibration process for area variations needs to be tested over more sites, preferably areas where the backscatter dependence on local incidence angle can be easily modeled and area effects can then be isolated. Such sites would most likely be bare earth or poorly vegetated since vegetation introduces complex backscattering behavior dependent on both ground slope and incidence angle. Also, steeper terrain would allow for more noticeable calibration discrepancies between heteromorphic and homomorphic techniques and could lend insight into opportunities to improve upon the projection angle technique.

With regards to the Fourier based method for estimating calibration error, more reference power spectra and their associated line fit parameters need to be computed for a wider range of slopes and terrain relief. This can be accomplished two ways: 1) download high resolution lidar data over more test sites and use the average terrain slope and line fit parameters to update the database for reference power spectra; or 2) create one large dataset constructed from individual circular transects from a variety of test sites and sort the transects by the mean slope within the circle. With the second method, the full range of terrain slopes would be more quickly covered, and a function could potentially be fit to the data to form a relationship between terrain slope and the E and α parameters. More transects from different test sites would then just smooth the average power spectrum for a given terrain slope.

While it was not the main goal for this work, the biomass estima-

tion process can be significantly improved. The most evident improvement is incorporation of radiometric calibration for local incidence angle effects. As previously discussed, the incidence angle calibration can be site, tree type, and polarization dependent. The most straightforward way to model the incidence angle dependence would be to take transects of backscatter data in the range direction and plot the results vs. incidence angle. The backscattering model that provided the best fit could then be used to remove the incidence angle effects from the SAR image. Care would need to be taken to ensure that the transects were extracted from mainly homogeneous forest stands and did not include contributions from artificial ground targets and strong point reflectors. Even after removal of incidence angle effects, there are still effects from speckle noise, geolocation errors, moisture, dihedral scattering from non-zero ground slopes, et al. Many of these factors are still poorly understood and prevent the pure geometrical isolation of the scattering from tree canopies.

Appendix

0.1 Facet Model Implementation

The detailed step-by-step approach to implementing the facet model correction for both satellite and airborne data is as follows:

- Determine the range and azimuth coordinates for each DEM pixel:
  - Satellite data [12]: For satellite data, orbit information is usually provided by the vendor. The orbit information is used in conjunction with the viewing geometry, timing information, and DEM coordinates to determine range and azimuth coordinates. Once the orbit information and the DEM share the same coordinate system and datum, a polynomial is fit through each element of the state vector. In other words, polynomial coefficients are estimated for each position direction:

$$x_{est} = p_{x,n}t^n + p_{x,n-1}t^{n-1} + p_{x,n-2}t^{n-2} \dots$$
$$y_{est} = p_{y,n}t^n + p_{y,n-1}t^{n-1} + p_{y,n-2}t^{n-2} \dots$$
$$z_{est} = p_{z,n}t^n + p_{z,n-1}t^{n-1} + p_{z,n-2}t^{n-2} \dots$$

    and similarly for the velocities. For this work, an 8-th order polynomial provided the necessary accuracy.

    Afterwards, for each DEM pixel, the azimuth and range bins that the pixel should be assigned to are iteratively solved for. Using a first guess of t_a, the azimuth time, a correction factor α is estimated

which updates the estimate of t_a until α falls under a specified tolerance.

$$\underline{l} = \underline{R}_{pixel} - \underline{R}_{sat} \text{ (Look vector)}$$
$$f_d = \frac{2\,(\underline{V}_{sat} \cdot \underline{l})}{\lambda \|\underline{l}\|} \text{ (Current doppler frequency)}$$
$$f_r = \frac{-2V_r^2}{\lambda \|\underline{l}\|} \text{ (Doppler chirp rate, } V_r \text{ - effective radar velocity)}$$
$$\alpha = -\frac{f_d}{f_r}$$
$$t_a = t_a + \alpha$$

Once convergence is reached on an estimate of t_a, the azimuth line would be

$$\text{azimuth} = \frac{ta - t_0}{\Delta t}$$

where t_0 is the time for the first line and Δt is the time spacing for each line. The range bin would then be

$$\text{range} = \frac{\|\underline{l}\| - R_0}{\Delta R}$$

where R_0 is the initial slant range and ΔR is the range pixel spacing.

– Airborne data [20]: The most well-known North American airborne SAR platforms in the last two decades are AirSAR/TopSAR and UAVSAR, both JPL operated systems. For both, very little positioning information is provided. However, since the data is acquired on an airborne platform, map coordinates can be converted to radar coordinates by using an SCH transformation. The SCH

system is spherical and is chosen to best approximate the ellipsoid in the along track direction. The SCH directions are: i) S - along track direction, ii) C - cross track direction, iii) H - height above approximating sphere.

The first step is to compute the parameters for the peg point, which is the nadir point of the aircraft during the middle of the data take. The peg point has a latitude θ_0, longitude λ_0, and heading η. The entire SCH transformation is dependent on those three values only. The peg point is where the approximating sphere for the SCH coordinates is defined, and the radius of the sphere is defined as:

$$r_a = \frac{r_e(\lambda_0) r_n(\lambda_0)}{r_e(\lambda_0)\cos^2(\eta) + r_n(\lambda_0)\sin^2(\eta)}$$

where $r_e(\lambda)$ and $r_n(\lambda)$ are the principal radii of curvature with the following form:

$$r_e(\lambda) = \frac{a}{\left(1 - e^2\sin^2(\lambda)\right)^{\frac{1}{2}}}$$

$$r_n(\lambda) = \frac{a(1-e^2)}{\left(1 - e^2\sin^2(\lambda)\right)^{\frac{3}{2}}}$$

The Cartesian WGS-84 coordinates (x,y,z) for the peg point are:

$$P = \begin{bmatrix} r_e(\lambda_0)\cos(\lambda_0)\cos(\theta_0) \\ r_e(\lambda_0)\cos(\lambda_0)\sin(\theta_0) \\ r_e(\lambda_0)(1-e^2)\sin(\lambda_0) \end{bmatrix}$$

The second step is to compute the Cartesian (x,y,z) coordinates for a given geographic DEM pixel (λ, θ, h):

$$\begin{bmatrix} x \\ y \\ z \end{bmatrix} = \begin{bmatrix} (r_e(\lambda) + h)\cos(\lambda)\cos(\theta) \\ (r_e(\lambda) + h)\cos(\lambda)\sin(\theta) \\ (r_e(\lambda)(1-e^2) + h)\sin(\lambda) \end{bmatrix}$$

Then, an intermediate reference system centered at the middle of the approximating sphere can be defined (x',y',z'): i) x' - normal direction to approximating sphere, ii) y' - tangent vector to reference curve, iii) z' - cross track direction. The DEM coordinates in this intermediate reference system can be determined through a combination of rotation and translation operations:

$$\begin{bmatrix} x' \\ y' \\ z' \end{bmatrix} = M_{ENU}^{x'y'z'} M_{xyz}^{ENU} \left(\begin{bmatrix} x \\ y \\ z \end{bmatrix} - P + r_a U \right)$$

where M_b^c is a transformation matrix from frame b to c, U is the x' direction defined in the Cartesian system, and ENU is a topographic frame defined as (E - East, N - North, U - Up). The transformation matrices are as follows:

$$M_{ENU}^{x'y'z'} = \begin{bmatrix} 0 & 0 & 1 \\ \sin(\eta) & \cos(\eta) & 0 \\ -\cos(\eta) & \sin(\eta) & 0 \end{bmatrix}$$

$$M_{xyz}^{ENU} = \begin{bmatrix} -\sin(\theta_0) & \cos(\theta_0) & 0 \\ -\sin(\lambda_0)\cos(\theta_0) & -\sin(\lambda)\sin(\theta_0) & \cos(\lambda_0) \\ \cos(\lambda_0)\cos(\theta_0) & \cos(\lambda_0)\sin(\theta_0) & \sin(\lambda_0) \end{bmatrix}$$

The next step is to convert the (x',y',z') coordinates into SCH coordinates using the following relations:

$$\begin{bmatrix} x' \\ y' \\ z' \end{bmatrix} = \begin{bmatrix} (r_a + h)\cos(c_\lambda)\cos(s_\theta) \\ (r_a + h)\cos(c_\lambda)\sin(s_\theta) \\ (r_a + h)\sin(c_\lambda) \end{bmatrix}$$

where $c_\lambda = C/r_a$ and $s_\theta = S/r_a$. The S values can be converted into an azimuth bin:

$$\text{azimuth} = \frac{S - S_0}{\Delta az}$$

where Δaz is the azimuth spacing of the data and S_0 is the S coordinate of the first line of the radar data, which is specified by JPL in the annotation file. The range bin can be found from the C coordinate using the law of cosines:

$$\text{range} = \frac{1}{\Delta R}\left(\sqrt{\begin{array}{c}(r_a+h)^2+(r_a+h_p)^2\\-2(r_a+h)(r_a+h_p)\cos(C/r_a)\end{array}} - R_0\right)$$

where h_p is the average height of the aircraft/sensor, also specified by the JPL annotation file.

- Compute the slope, aspect, and local incidence angle (see Chapter 2)
- Estimate area in map coordinates using slope
  - For a particular map pixel, the area can be estimated using the slope:

$$\text{area} = \frac{\Delta DEM^2}{\cos(S)}$$

    where ΔDEM is the DEM pixel spacing in meters.

- Resample area estimate to radar coordinates using bilinear weighting distribution
  - Once the area for a pixel has been estimated in map coordinates, the area needs to be resampled to radar coordinates. A bilinear weighting model is used to distribute the area estimates over the appropriate radar pixels. Each DEM pixel has a fractional range

bin r and an azimuth line a. Therefore, the integer bounds in the radar image become:

$$r_1 = \text{floor}(r)$$

$$r_2 = \text{ceil}(r)$$

$$a_1 = \text{floor}(a)$$

$$a_2 = \text{ceil}(a)$$

The integer bounds are used as array indices for the area image in radar coordinates. The bilinear distribution is performed as follows:

$$A_{a_2,r_2} = A_{a_2,r_2} + (r - r_1)(a - a_1) * \text{area}$$

$$A_{a_2,r_1} = A_{a_2,r_1} + (r_2 - r)(a - a_1) * \text{area}$$

$$A_{a_1,r_2} = A_{a_1,r_2} + (r - r_1)(a_2 - a) * \text{area}$$

$$A_{a_1,r_1} = A_{a_1,r_1} + (r_2 - r)(a_2 - a) * \text{area}$$

where A is the area image in radar coordinates and the quantity (area) is as computed in the previous step. Additionally, a nearest neighbor approach is used to assign the incidence angle estimate to a radar coordinate which will then be averaged during the correction.

- Normalize intensity image for area and (optionally) local incidence angle
  - To correct the intensity image in radar coordinates, the following formula is applied:

$$\sigma^0 = \beta^0 \frac{A_{ref}}{A}$$

where σ^o is the normalized intensity, β is the uncorrected intensity, and A_{ref} is the reference area determined from the default range and azimuth pixel spacing. An additional correction for backscatter variation due to local incidence angle can be applied with the following form:

$$\sigma^0 = \beta^0 \frac{A_{ref}}{A} \cos(\theta_l)$$

This correction is often called a "gamma" correction. Typically, the backscatter variation with local incidence angle is dependent on scatter type, and other powers of cosine have been used in the literature [24].

Bibliography

[1] *Principles and Applications of Imaging Radar: Manual of Remote Sensing*, volume 2. John Wiley and Songs, Inc., third edition, 1998.

[2] Bartlett experimental forest, April 2010. `http://www.fs.fed.us/ne/durham/4155/bartlett.htm`.

[3] Uavsar data format for standard polarimetric products, May 2010. `http://uavsar.jpl.nasa.gov/doc/dataformat.htm`.

[4] J. Anderson, M.E. Martin, M-L. Smith, R.O. Dubayah, M.A. Hofton, P. Hyde, B.E. Peterson, J.B. Blair, and R.G. Knox. The use of waveform lidar to measure northern temperate mixed conifer and deciduous forest structure in New Hampshire. *Remote Sensing of Environment*, 105:248–261, 2006.

[5] M.M. Ansoult. Circular sampling for Fourier analysis of digital terrain data. *Mathematical Geology*, 21(4), 1989.

[6] T. Bayer, R. Winter, and G. Schreier. Terrain influences in SAR backscatter and attempts to their correction. *IEEE Transactions on Geoscience and Remote Sensing*, 29(3), May 1991.

[7] A. Beaudoin, N. Stussi, D. Troufleau, N. Desbois, L. Piet, and M. Deshayes. On the use of ERS-1 SAR data over hilly terrain: necessity of

radiometric corrections for thematic applications. In *Proc. of IEEE-IGARS'95*, July 1995.

[8] J.B. Blair, D.L. Rabine, and M.A. Hofton. The Laser Vegetation Imaging Sensor (LVIS): a medium-altitude, digitisation only, airborne laser altimeter for mapping vegetation and topography. *ISPRS Journal of Photogrammetry and Remote Sensing*, 54:115–122, 1999.

[9] C.C. Carabajal and D.J. Harding. ICESat validation of SRTM C-band digital elevation models. *Geophysical Research Letters*, 32(L22S01), 2005.

[10] J.M. Chen and J. Cihlar. Retrieving leaf area index of boreal conifer forests using Landsat TM images. 55(2):153–162, February 1996.

[11] B.D. Cook, G. Sun, K.J. Ranson, P.M. Montesano, S.B. Luthcke, and J.B. Blair. Accuracy of DESDynI biomass estimates using lidar and data fusion methods. In *American Geophysical Union, Fall Meeting 2009*, December 2009.

[12] J.C. Curlander and R. McDonough. *Synthetic aperture radar: Systems and signal processing.* Wiley Series in Remote Sensing, 1991.

[13] K.L. Denman, G. Brasseur, A. Chidthaisong, P. Ciais, P.M. Cox, R.E. Dickinson, D. Hauglustaine, C. Heinze, E. Holland, D. Jacob, U. Lohmann, S. Ramachandran, P.L. da Silva Dias, S.C. Wofsy, and X. Zhang. Couplings between changes in the climate system and biogeochemistry. In

Climate Change 2007: The Physical Science Basis. Contribution of Working Group I to the Fourth Assessment Report of the Intergovernmental Panel on Climate Change, Cambridge, UK and New York, NY, USA. Cambridge University Press.

[14] G. Falorni, V. Teles, E.R. Vivoni, R.L. Bras, and K.S. Amaratunga. Analysis and characterization of the vertical accuracy of digital elevation models from the Shuttle Radar Topography Mission. *Journal of Geophysical Research*, 110, 2005.

[15] P. Frederiksen, O. Jacobi, and K. Kubik. Accuracy prediction for digital elevation models. In *XV Congress of the International Society for Photogrammetry and Remote Sensing*, Rio de Janeiro, Brazil, 1994.

[16] A. Freeman, P. Rosen, R. Jordan, W. Johnson, S. Hensley, T. Sweeter, A. Loverro, J. Smith, G. Sprague, and Y. Shen. DESDYNI - a NASA mission for ecosystem, solid earth, and cryosphere science. In *Proc. of 4th Int. Workshop on Science and Applications of SAR Polarimetry and Polarimetric Interferometry*, January 2009.

[17] V.I. Kharuk G. Sun, K.J. Ranson. Radiometric slope correction for forest biomass estimation from SAR data in the Western Sayani Mountains, Siberia. *Remote Sensing of Environment*, 79, 2002.

[18] R. Gutierrez, A. Neuenschwander, and M.M. Crawford. Development of laser waveform digitization for airborne LIDAR topographic mapping instrumentation. *IEEE*, 2005.

[19] S. Hensley. Interoffice memorandum: DESDynI biomass error model and associated spreadsheet, March 2010.

[20] S. Hensley, E. Chapin, A. Freedman, and T. Michel. Improved processing of AIRSAR data based on the GeoSAR processor.

[21] S. Hensley, T. Michel, M. Simard, C. Jones, R. Muellerschoen, C. Le, H. Zebker, and B. Chapman. Residual motion estimation for UAVSAR: implications of an electronically scanned array, 2009.

[22] R.A. Houghton. Aboveground forest biomass and the global carbon balance. *Global Change Biology*, 11:945–958, 2005.

[23] P. Hyde, R. Dubayah, W. Walker, J.B. Blair, M. Hofton, and C. Hunsaker. Mapping forest structure for wildlife habitat analysis using multi-sensor (LIDAR, SAR/InSAR, ETM+, Quickbird) synergy. *Remote Sensing of Environment*, 102:63–73, 2006.

[24] G. Leclerc, N. Beaulieu, and F. Bonn. A simple method to account for topography in the radiometric correction of radar imagery. *International Journal of Remote Sensing*, 22(17):3553–3570.

[25] M.A. Lefsky, W.B. Cohen, D.J. Harding, G.G. Parker, S.A. Acker, and S.T. Gower. Lidar remote sensing of above-ground biomass in three biomes. *Global Ecology and Biogeography*, 11:393–399, 2002.

[26] R.M. Lucas, N. Cronin, A. Lee, M. Moghaddam, C. Witte, and P. Tickle. Empirical relationships between AIRSAR backscatter and LIDAR-derived

forest biomass, Queensland, Australia. *Remote Sensing of Environment*, 100:407–425, 2006.

[27] A. Luckman, J. Baker, T.M. Kuplich, C.C.F. Yanasse, and A.C. Frery. A study of the relationship between radar backscatter and regenerating tropical forest biomass for spaceborne SAR instruments. *Remote Sensing of Environment*, 60:1–13, 1997.

[28] A. Luckman, J.R. Baker, M. Honzak, and R. Lucas. Tropical forest biomass density estimation using JERS-1 SAR: seasonal variation, confidence limits and application to image mosaics. *Remote Sensing of Environment*, 63(2):126–139, 1998.

[29] A.J. Luckman. The effects of topography on mechanisms of radar backscatter from coniferous forest and uplanld pasture. *IEEE Transactions on Geoscience and Remote Sensing*, 36(5), September 1998.

[30] L. Pierce, J. Kellndorfer, W. Walker, and O. Barros. Evaluation of the horizontal resolution of SRTM elevation data. *Photogrammetric Engineering & Remote Sensing*, 72(11):1235–1244, November 2006.

[31] K.J. Ranson, G. Sun, J.F. Weishampel, and R.G. Knox. Forest biomass from combined ecosystem and radar backscatter modeling. *Remote Sensing of Environment*, 59:118–133, 1997.

[32] E.J. Rignot, R. Zimmermann, and J.J. van Zyl. Spaceborne applications

of P band imaging radars for measuring forest biomass. *IEEE Transactions on Geoscience and Remote Sensing*, 33(5), September 1995.

[33] E. Rodríguez, C.S. Morris, and J.E. Belz. A global assessment of the SRTM performance. *Photogrammetric Engineering & Remote Sensing*, 72(3):249–260, March 2006.

[34] S. Saatchi, K. Halligan, D.G. Despain, and R.L. Crabtree. Estimation of forest fuel load from radar remote sensing. *IEEE Transactions on Geoscience and Remote Sensing*, 45(6), 2007.

[35] S. Saatchi, K. Halligan, D.G. Despain, and R.L. Crabtree. Estimation of forest fuel load from radar remote sensing. *IEEE Transactions on Geoscience and Remote Sensing*, 45(6), 2007.

[36] J.B. Sankey, N.F. Glenn, M.J. Germino, A.I.N. Gironella, and G.D. Thackray. Relationships of aerolian erosion and deposition with LiDAR-derived landscape surface roughness following wildfire. *Geomorphology*, 2010.

[37] D. Small, N. Miranda, and E. Meier. Local incidence angle considered harmful. CEOS SAR Calibratin/Validation Workshop, November 2009.

[38] David Small, Francesco Holecz, Erich Meier, and Daniel Nesch. Absolute radiometric correction in rugged terrain: A plea for integrated radar brightness. In *Proc. of IGARSS98*, pages 6–10, 1998.

[39] B. Smith and D. Sandwell. Accuracy and resolution of shuttle radar topography mission data. *Geophysical Research Letters*, 30(9), 2003.

[40] T.L. Toan, S. Quegan, I. Woodward, M. Lomas, N. Delbart, and G. Picard. Relating radar remote sensing of biomass to modelling of forest carbon budgets. *Climatic Change*, 67:379–402, 2004.

[41] L.M.H. Ulander. Radiometric slope correction of Synthetic-Aperture radar images. *IEEE Transactions on Geoscience and Remote Sensing*, 34(5), September 2002.

[42] J. van Zyl. The shuttle radar topography mission (SRTM): a breakthrough in remote sensing of topography. *Acta Astronautica*, 48(5-12):559–565, 2001.

[43] Q. Zhou and X. Liu. Error analyais on grid-based slope and aspect algorithms. *Photogrammetric Engineering and Remote Sensing*, 70(8), August 2004.